Dark Energy Contaminated Black Hole Solution: A Drive Through the Thermodynamic Properties

Promila Biswas * ¹, Subhajit Pal *², Sukanya Dutta ** ³, Ritabrata Biswas ** ⁴ and Farook Rahaman* ⁵

*Department of Mathematics, Jadavpur University, Kolkata-32, India **Department of Mathematics, The University of Burdwan, Burdwan-713104, India

Abstract

We investigate the evolution of black hole mass within a cosmological background modeled by a Modified Chaplygin Gas (MCG) under various dark energy equation of state parametrizations, including Linear, Logarithmic, CPL, JBP, FSLL-II, and Barboza–Alcaniz (BA) models. The logarithmic mass ratio $\log_{10}[M(z)/M_0]$ is found to be highly sensitive to the redshift-dependent evolution of $\omega(z)$, with gentle slopes in Linear, Logarithmic, and CPL models indicating quasistatic accretion, steep slopes in JBP corresponding to rapid late-time variations, and non-monotonic behaviour in FSLL-II and BA highlighting transient suppression or enhancement of accretion due to repulsive dark energy effects. Peaks, minima, and amplitude offsets in the mass ratio reflect the dynamic interplay between horizon thermodynamics, the evolving pressure of the MCG, and cosmic expansion, illustrating how the black hole mass growth is directly influenced by both the temporal evolution of dark energy and the effective gravitational potential of the surrounding cosmic fluid. Our results demonstrate that black hole accretion acts as a sensitive probe of the time-dependent cosmic pressure landscape and provides physical insights into the coupling between local strong gravity and global accelerated expansion.

Keywords: Accretion, Dark energy, Black hole, Thermodynamics, Cosmological Parametrisation.

PACS No.: 95.36.+x, 04.70.-s, 97.10.Gz, 98.80.-k, 05.70.-a.

1 Introduction

Dark energy (DE) is a theoretical form of energy that permeates all of space and accelerates the present day expansion of the universe. For a homogeneous, isotropic universe, the Friedmann Lemaitre Robertson Walker (FLRW) metric

$$ds^{2} = -dt^{2} + a(t)^{2} \left[\frac{dr^{2}}{1 - \kappa r^{2}} + r^{2} d\Omega^{2} \right] , \qquad (1)$$

 $^{^{1}}$ promilabiswas8@gmail.com ; Orchid : 0009 - 0004 - 1431 - 3857

 $^{^{2}}$ subhajitpal968@gmail.com ; Orchid : 0009 - 0002 - 2431 - 1375

 $^{^{3}}$ sduttasukanya@gmail.com ; Orchid : 0009 - 0004 - 2989 - 309X

⁴biswas.ritabrata@gmail.com ; Orchid : 0000 - 0003 - 3086 - 892X

 $^{^{5}}$ farookrahaman@gmail.com ; Orchid : 0000 - 0003 - 0594 - 4783

where $\kappa = 0, +1, -1$ corresponds to flat, closed or open universe respectively. $d\Omega^2 = d\theta^2 + \sin^2\theta \ d\phi^2$. From the Einstein's field equation $G_{\mu\nu} = 8\pi G_N T_{\mu\nu}$, the Friedmann equations turn to be

$$H^{2} = \left(\frac{\dot{a}}{a}\right)^{2} = \frac{8\pi G_{N}}{3}\rho_{tot} - \frac{\kappa}{a^{2}} + \frac{\Lambda}{3} \quad \text{and}$$
 (2)

$$\frac{\ddot{a}}{a} = -\frac{4\pi G_N}{3} \left(\rho_{tot} + 3p_{tot}\right) + \frac{\Lambda}{3} \quad , \tag{3}$$

where H is the Hubble parameters, ρ_{tot} and p_{tot} are density and pressure of universe.

Rewriting equation (2) as,

$$H^{2} = \frac{8\pi G_{N}}{3} \left(\rho_{b} + \rho_{de} + \rho_{r}\right) + \frac{\Lambda}{3} - \frac{\kappa}{a^{2}} \quad , \tag{4}$$

where ρ_b , ρ_{DE} and ρ_{rad} are respectively the density contribution by baryons, DE and radiation. For expansion rate, we define

$$E^{2}(z) \equiv \frac{H^{2}(z)}{H_{0}^{2}} = \Omega_{b0}(1+z)^{3} + \Omega_{de0}F(z) + \Omega_{r0}(1+z)^{4} + \Omega_{\kappa 0}(1+z)^{2} + \Omega_{0} \quad , \tag{5}$$

where Ω_{b0} , Ω_{DE0} , Ω_{r0} , $\Omega_{\kappa 0}$ and Ω_{0} are present day dimensionless densities given as

$$\Omega_i \equiv \frac{8\pi G_N}{3H^2} \rho_i \quad i = \text{rad, DE and DM} \quad .$$
(6)

Due to curvature, the contribution is

$$\Omega_{\kappa} \equiv -\frac{\kappa}{H^2 a^2} \tag{7}$$

and for cosmological constant,

$$\Omega_0 \equiv \frac{\Lambda}{3H_0^2} \quad . \tag{8}$$

F(z) will be determined according to the model of DE chosen.

As E(z=0)=1 at the present epoch, we obtain

$$\Omega_{b0} + \Omega_{DE0} + \Omega_{r0} + \Omega_{\kappa 0} + \Omega_0 = 1 \qquad , \tag{9}$$

where Ω_{b0} , Ω_{DE0} , Ω_{r0} and $\Omega_{\kappa 0}$ are present time values of dimensionless densities. Depending upon this model, we will establish a tool to measure Hubble parameter at different redshifts. In section 3, such data points will be incorporated.

In cosmology, DE is often modelled as a perfect fluid with an equation of state (EoS)

$$p = \omega \rho \quad , \tag{10}$$

where p, ω and ρ are the pressure of the DE candidate, EoS parameter and energy density respectively. Friedmann equation $\frac{\ddot{a}}{a} = -\frac{4\pi G_N}{3}(\rho + 3p)$ (where $a \equiv a(t)$ is the scale factor, overdot signifies derivative with respect to time) for accelerated expansion ($\ddot{a} > 0$) leads us to the condition $\rho + 3p < 0$, i.e, $\omega < -\frac{1}{3}$.

Einstein field equations with the cosmological constant Λ is one way to model DE is written as,

$$G_{\mu\nu} + \Lambda g_{\mu\nu} = \frac{8\pi G_N}{c^4} T_{\mu\nu} \quad , \tag{11}$$

where $G_{\mu\nu}$, $g_{\mu\nu}$ and $T_{\mu\nu}$ are Einstein tensor (curvature of space-time), metric tensor and energy momentum tensor respectively. Energy density associated with the cosmological constant is

$$\rho_{\Lambda} = \frac{\Lambda c^2}{8\pi G_N} \quad , \tag{12}$$

which remains constant over time, unlike the matter or radiation whose densities dilute as the universe expands. Cosmic coincidence problem, fine tuning etc were not justified by the cosmological constant and dynamical dark energy models were required to be introduced.

The modified Chaplygin gas (MCG) is a theoretical model in cosmology that aims to unify dark matter(DM) and DE into a single fluid. Described by the equation of state

$$p = A\rho - \frac{B}{\rho^d} \quad , \tag{13}$$

it behaves like matter or radiation in the early universe and mimics DE at late times, thus explaining both cosmic structure formation and accelerated expansion. Its flexibilities allow it to fit observational data from supernovae [1]. The cosmic microwave background and large scale structure, making it a compelling alternative to the standard Λ CDM model. In equation (13), A and d will satisfy the condition of being non-negative, A and B are considered as constants in the adiabatic process[2]. For specific values of the parameters, the MCG will be transformed to alternative model of DM and DE. On the other hand, the generalised Chaplygin gas (GCG) concept can be converted from the conditions d>1 and A=0 to $p=-\frac{B}{\rho^d}$. However, the MCG will degenerate into a straightforward pure Chaplygin gas (CG): $p=-\frac{B}{\rho}$, which accurately describes the aerodynamic process that produces lifting forces on an aircraft's wing, if the parameters meet the requirements d=1 and A=0. In section 2, we will recall a black hole (BH) solution which is embedded in MCG environment.

Black holes (BHs) are known to accrete matter and radiation. Babichev et al. (2004) [3] showed that BHs can accrete a perfect fluid with negative pressure. If DE behaves like a fluid with $\omega < -1$ (phantom energy), it could cause BHs to loose mass over time which is contrary to usual accretion. For $-1 < \omega < -\frac{1}{3}$ (quintessence), BHs may still gain mass except a comparatively slow rate. Nayak and Singh (2011) studied the evolution of primordial BHs within the Brans-Dicke theory, incorporating phantom energy accretion [4]. Their findings indicated that radiation accretion increases the life time of these BHs, whereas phantom energy accretors accrete their evaporation. He et al analysed the quasi normal modes of BHs absorbing DE. They found that the accretion of phantom energy could lead to growing modes in the perturbation tail, indicating potential instabilities. De Prolis, Jamil and Qadir [5] explored the effects of accreting viscous phantom energy onto Schwarzschild BHs. Their study revealed that bulk viscosity accelerates the mass loss of BHs compared to non viscous accretion, suggesting that the inclusion of viscosity in DE models can significantly alter BH dynamics. Jamil, Qadir and Rashid [6] investigate charged BHs in a phantom environment. They find that the accretion of phantom DE onto a charged BH could eventually lead to the formation of a naked singularity.

Though DE does not directly couple to baryonic matter, interaction between DE and DM can still indirectly affect baryons by modifying the gravitational potential of DM halos which govern how baryons fall in and cool to form stars and galaxies. Since DM potential will define the gravitational environment for baryons, any evolution in DM density profiles due to DE-DM interaction can affect gas accretion rate, cooling efficiency of baryonic gas, star formation rates (SFRs), especially in early galaxies, etc. In other concepts, if

DE transfers energy to DM, i.e., a positive coupling takes place, DM becomes effectively "heavier", deepening the potential well and drawing in more baryons. Conversely, energy flow from DM to DE, if a negative coupling takes place, reduces the potential depth, making baryonic collapse less efficient. Change in halo potential affects supernova feedback, outflows and baryon retention. A shallower potential due to interaction might allow easier expansion of gas, suppressing star formation in low mass halos. Observationally, these can lead to altered baryonic Tully-Fisher relation which links baryon mass to rotation speed. Impacts on stellar to halo mass relation and galaxy halo connection statistics are found. These models provide better fits to dwarf galaxy dynamics which show deviation from Λ CDM expectations.

Accretion occurs when a gravitational object like a BH interacts with a surrounding medium. For DE, this interaction depends on its energy-momentum flow, governed by GR.

For a perfect fluid with

$$T_{\mu\nu} = (\rho + p)u_{\mu}u_{\nu} + pg_{\mu\nu}$$
 (14)

If $\rho + p > 0$, i.e., for normal or quintessence like DE, the BH mass. On the other hand, if $\rho + p < 0$, i.e., for phantom DE, the BH looses mass due to a negative effective energy flux into the BH. If the chosen DE model is a scalar field, it can have spatial and temporal variation. in such models, DE has a non trivial energy flux, allowing it to accrete onto BHs. If DE dominates the cosmic fluid and a BH is embedded in such a background (e.g. Schwarzschild-deSitter on MeVittie space-time), accretion becomes theoretically feasible.

$$\rho_{DE}(z) = \rho_{DE,0} \times \exp\left\{3 \int_{0}^{z} \frac{1 + \omega(z')}{1 + z'} dz'\right\}$$
 (15)

Current observations points towards time-varying DE models. Redshift parameterizations $(p(z) = \omega(z)\rho(z))$ provide a phenomenological, model-independent way to describe DE. Instead of assuming a specific field or potential (like quintessence), we explore the possible behaviours of $\omega(z)$ directly from data. Some parameterizations (like JBP or BA) are designed to behave well at both low and high redshift. Predictive power, i.e., to reveal the possible future of the universe is an addon utility of such models.

We enlist several redshift parametrisation models in the table 2. In the second column we recall their EoS-s. We analyze them for the data set noted in table 1 and constrain the free parameters and the best fits are noted in the 3rd column of table 2.

Studies regarding the accretion onto a BH which carries DE contamination in its metric results wind curves of radial velocity to end at different distances from the central compact object. This reduces the extremity of DE accretion onto Kerr metric which predicts radial inward speed wind to be equal to the speed of light at a finite distance. In this work, a DE contaminated black hole solution will be chosen and affect on its mass will be followed. The DE candidate which affects from the BH metric itself and the candidates which will be modelled to accrete are dynamical. Variations of BH mass with respect to redshift will be studied. We will follow how the ratio of the mass to present day mass does change.

In the next section (section 2), we will recall a BH solution which is sitting in the MCG filled universe. In section 3, we will collect and enlist $H(z) - z - \sigma(z)$ data points and constrain some redshift parameterization type DE models. In Section 4, Accretion of previously constrained DE models onto the MCG contaminated BH will be studied. Finally, we will conclude this article in section 6.

2 Black Hole Solution Contaminated by Modified Chaplygin Gas

For vacuum, i.e., absence of matter or radiation leads to $T_{\mu\nu} = 0$, i.e., $R_{\mu\nu} = \Lambda g_{\mu\nu}$ which governs the vacuum geometry in the presence of DE. The vacuum solution with $\Lambda > 0$ is popularly known as the deSitter space-time. The deSitter space is maximally symmetric with constant positive curvature, described in static co-ordinates as [c=1]

$$f_{dS} = \left(1 - \frac{\Lambda r^2}{3}\right) (17)$$

Here, a cosmological horizon appears at $r = \sqrt{\frac{3}{\Lambda}}$. No observer can access region beyond this. This horizon is not due to matter, but purely due to space-time expansion, which is a pure effect of DE.

A BH is a region in space-time where gravity is so intense that nothing, not even light can escape its inward pull. These compact objects are typically formed from the remnants of massive stars that collapse under their own gravity, BHs compress matter into an incredibly small region with infinite density, known as a singularity. Although BHs themselves are invisible, their presence is detected through the gravitational effects on nearby stars and gas[7], as well as by observing high energy radiation emitted by matter being pulled in.

Now, if a matter mass M is thought to be placed in deSitter space, we reach at the Schwarzschild-deSitter (SdS) metric given by equation (16) with the lapse function

$$f_{SdS}(r) = 1 - \frac{2G_N M}{r} - \frac{\Lambda r^2}{3}$$
 (18)

The second term in equation (18) is gravitational attraction and the last one is the repulsion due to DE. Here, we find two horizons, viz., BH event horizon(r_{bh}) and cosmological horizon (r_c). At small radial distance, gravity dominates and at large radial distance, DE dominates. The region between r_{bh} and r_c is static and observable. However, two horizons lead to two surface gravities, i.e., two different temperatures and different thermodynamic properties are evolved.

If now, we opt Reissner-Nordstrom-deSitter (RNdS) BH, lapse function of this spherically symmetric, charged BH comprising a cosmological constant looks like

where
$$f_{RNdS}(r) = 1 - \frac{2G_N M}{r} + \frac{G_N Q^2}{4\pi\epsilon_0 r^2} - \frac{\Lambda r^2}{3}$$
, (19)

where Q is electric charge and ϵ_0 is the electric constant. A vanishing lapse function gives upto three real positive roots, corresponding to inner(Cauchy) horizon r_- , outer Cauchy horizon r_+ and cosmological horizon r_c . A condition $r_- < r_+ < r_c$ occurs for specific ranges of M, Q and Λ . High charge on small mass lead to a naked singularity[8].

Moving one step ahead, Kerr deSitter, i.e., rotating BH in deSitter space can be written. Besides three horizons mentioned earlier, ergospheres can be obtained. These ergospheres' sizes and shapes can get affected by Λ as well[9].

Including quintessence in Schwarzschild or Reissner-Nordstrom solutions, Kiselev BH is proposed with the lapse function $(G_N = 1)$

$$f_{Kiselev}(r) = 1 - \frac{2M}{r} - \frac{c}{r^{3\omega + 1}} \quad , \tag{20}$$

when $\omega = -1$, we are back to the deSitter background (18). Using Newmann-Janis algorithm, rotating, rotating Kiselev BHs are calculated by Ghosh et al[10, 11].

Now, we will recall a BH solution which is contaminated by the presence of MCG. The action is chosen as [12]

$$\mathcal{I} = \frac{1}{16\pi} \int d^4x \sqrt{-g} \left[R + 6\ell^{-2} - \frac{1}{4} F_{\mu\nu} F^{\mu\nu} \right] + \mathcal{I}_M \quad , \tag{21}$$

where R, $g_{\mu\nu}$, $g=det(g_{\mu\nu})$ and ℓ represent the Ricci scalar, the metric tensor, determinant of the metric tensor and the AdS length respectively. $F_{\mu\nu}=\partial_{\mu}A_{\nu}-\partial_{\nu}A_{\mu}$ gives the field strength of the electromagnetic field with A_{μ} being the gauge potential. \mathcal{I}_{M} indicated the matter contribution due to the MCG background.

The following field equations result from changing the action (21):

$$G_{\mu\nu} - \frac{3}{\ell}g_{\mu\nu} = T_{\mu\nu}^{EM} + T_{\mu\nu}^{MCG}$$
 and (22)

$$\partial_{\mu} \left(\sqrt{-g} F^{\mu\nu} \right) = 0 \quad , \tag{23}$$

the Einstein tensor $G_{\mu\nu}$ with $T_{\mu\nu}^{MCG}$ indicates the energy-momentum tensor for MCG, while $T_{\mu\nu}^{EM}$ denotes the specific formulation of the energy momentum tensor for the electromagnetic field

$$T_{\mu\nu}^{\rm EM} = 2\left(F_{\mu\lambda}F_{\nu}^{\ \lambda} - \frac{1}{4}g_{\mu\nu}F^{\lambda\delta}F_{\lambda\delta}\right) \quad . \tag{24}$$

Here, we consider a four-dimensional space-time which is static and exhibits spherical symmetry as the equation (16).

Our purpose is to determine the excitation for the energy density in a minute way. Hence we use the metric function in equation (16) and applying conservation conditions to the energy momentum tensor[13, 14], using the equation (13) and the equation of continuity

$$\dot{\rho} + 3\frac{\dot{a}}{a}(p+\rho) = 0 \quad , \tag{25}$$

we obtain

$$\rho^{d}\dot{\rho} + \frac{3\dot{a}}{a} \left[A\rho^{d+1} - B + \rho^{d+1} \right] = 0 \implies \frac{\rho^{d}\dot{\rho}}{\left[B - A\rho^{d+1} - \rho^{d+1} \right]} = \frac{3\dot{a}}{a} \quad . \tag{26}$$

Simplifying the above, we get,

$$\rho^d \dot{\rho} = -\frac{\dot{x}}{(A+1)(d+1)} \quad ,$$

where $x = B - A\rho^{d+1} - \rho^{d+1}$. Incorporating the value of $\rho^d \dot{\rho}$ in 23,

$$-\frac{\dot{x}}{(A+1)(d+1)x} = \frac{3\dot{a}}{a} \quad .$$

Integrating the above, we get the simplified version,

$$(A+1)\rho^{d+1} = B - \frac{C}{a^{3(A+1)(d+1)}} \quad , \tag{27}$$

where, C is the integrating constant. Assuming the value of $C = -\gamma^{(A+1)(d+1)}$ and incorporating the value of $a^3 = r[15]$, we finally obtain,

$$\rho(r) = \left\{ \frac{1}{1+A} \left(B + \left(\frac{\gamma}{r} \right)^{(1+A)(1+d)} \right) \right\}^{\frac{1}{1+d}} . \tag{28}$$

It is essential to use an integrating constant, represented as $\gamma > 0$. Notably, the energy density is limited to roughly $\left(\frac{B}{1+A}\right)^{\frac{1}{1+d}}$ [15]. In areas far from the BH, MCG behaves like a cosmological constant, but as it gets closer to the BH, it gradually shows signs of increased gravitational density.

According our density function and from (16), we get the value of the following

$$R = \frac{2 - 2f(r) - 4rf'(r) - r^2f''(r)}{r^2}, \ R_{00} = \frac{1}{2}f(r)\left\{\frac{2f'(r)}{r} + f''(r)\right\}, \ R_{11} = -\frac{2f'(r) + rf''(r)}{2rf(r)} \ \text{and} \ T_{00} = \rho c^2 \ .$$

Incorporating the above values in Einstein's field equation

$$R_{qy} - \frac{1}{2}Rg_{qy} = \frac{8\pi G}{c^4}T_{qy}$$

taking c=1, we can derive a concise expression for the analytical solution f(r) as

$$f_{MCG}(r) = 1 - \frac{2M}{r} + \frac{Q^2}{r^2} + \frac{r^2}{\ell^2} - \frac{r^2}{3} \left(\frac{B}{A+1}\right)^{\frac{1}{d+1}} {}_{2}F_{1}[\alpha, \nu; \lambda; \xi] \quad , \tag{29}$$

where M and Q indicate the BH's mass and charge respectively and the hyper-geometric function ${}_2F_1[\alpha,\nu;\lambda;\xi]$ can be expressed as a power series

$${}_{2}F_{1}[\alpha,\nu;\lambda;\xi] = \sum_{k=0}^{\infty} \frac{(\alpha)_{k}(\nu)_{k}/(\lambda)_{k}}{k!} \, \xi^{k}, \tag{30}$$

where $|\xi|$ < 1, the Pochhammer symbol is symbolized as $(n)_k$ [16], the parameter sets $(\alpha, \nu, \lambda, \xi)$ can be expressed as

$$\alpha = -\frac{1}{d+1}, \quad \nu = \frac{1}{1+A+d(A+1)}, \quad \lambda = 1+\nu, \quad \xi = -\frac{1}{B} \left(\frac{\gamma}{r}\right)^{(A+1)(d+1)}$$

3 Differential Ages Method : Collection of Hubble parameter vs Redshift data

From the definition of Hubble parameter at redshift z, i.e., $H(z) = \frac{\dot{a}}{a}$ and the relation between the redshift z and the scale factor a, $a = \frac{1}{1+z}$, differentiating with respect to cosmic time,

$$\frac{dz}{dt} = \frac{d}{dt}(1+z) = -\frac{\dot{a}}{a^2} = -\frac{H(z)}{a} = -H(z)(1+z) \implies H(z) = -\frac{1}{1+z}\frac{dz}{dt}$$

We are with fundamental equation of the different ages method. Since we cannot measure the exact derivative $\frac{dz}{dt}$ directly from observations, we use nearly data points to approximate it using finite differences. This gives

$$\frac{dz}{dt} \approx \frac{\Delta z}{\Delta t} \quad .$$

Ages are determined by stellar population synthesis models from galaxy spectra. For this, those galaxies are chosen which are massive, passively evolving (i.e., no significant star formation) and existing over a narrow redshift range. From this, classes of two galaxies are opted with redshift and age (z, t(z)) and $(z + \Delta z, t(z + \Delta z))$ (say) respectively. Then

$$H(z) \approx -\frac{1}{1+z} \cdot \frac{(z+\Delta z)-z}{t(z+\Delta z)-t(z)}$$

Assuming $\Delta z = z_2 - z_1 \ll 1$.

Since Hubble parameter estimate is a ratio, uncertainties Δt dominate the error bars

$$H(z) = -\frac{1}{1+z} \frac{\Delta z}{\Delta t} \implies \delta H(z) = \frac{1}{1+z} \frac{\Delta z}{\Delta t^2} \delta(\Delta t)$$

This is a direct measurement of H(z) unlike integral methods (SNe, BAO) that gives distances. No assumption of spatial flatness, DE model, etc. This differentiates well between different DE models through slope of H(z).

To check the uncertainty, we denote uncertainties in redshift and age difference respectively as $\sigma_{\Delta z}$ and $\sigma_{\Delta t}$ and obtain,

$$\sigma_H^2 = \left(\frac{\partial H}{\partial \Delta z}\right)^2 + \left(\frac{\partial H}{\partial \Delta t}\right)^2 \sigma_{\Delta t}^2 \quad .$$

Hence, the partial derivatives are calculated as

$$\frac{\partial H}{\partial \Delta z} = -\frac{1}{1+z} \frac{1}{\Delta z}$$
 and

$$\frac{\partial H}{\partial \Delta z} = \frac{1}{1+z} \frac{\Delta z}{\Delta t^2} \quad ,$$

leaving the total uncertainty as,

$$\sigma_H^2 = \left(\frac{1}{1+z}\frac{1}{\Delta t}\right)^2 \sigma_{\Delta z}^2 + \left(\frac{1}{1+z}\frac{\Delta z}{\Delta t^2}\right)^2 \sigma_{\Delta t}^2 \quad .$$

Using differential ages method, different Hubble parameter data are obtained which are enlisted in table 1.

Table 1: Hubble parameter H(z) with redshift and errors σ_H from Differential Ages method

	1		
Sl No.	Z	$H(z)$ with $\sigma_H(z)$	Ref
1	0	69.01 ± 1.30	[17]
2	0.07	69 ± 19.6	[18]
3	0.07	70.4 ± 20	[19]
4	0.09	69 ± 12	[20]
5	0.09	70.4 ± 12.2	[20]
6	0.1	69 ± 12	[21]
7	0.1	70.4 ± 12.2	[19]
8	0.12	68.6 ± 26.2	[18]
9	0.12	70 ± 26.7	[17]
10	0.17	83 ± 8	[21]
11	0.17	84.7 ± 8.2	[19]
12	0.179	75 ± 4	[22]
13	0.179	76.5 ± 4	[23]
14	0.199	76.5 ± 5.1	[23]
15	0.1993	75 ± 5	[22, 24]
16	0.2	72.9 ± 29.6	[18]
17	0.24	79.7 ± 2.7	[25]
18	0.27	70 ± 14	[20]
19	0.27	78.6 ± 14.3	[21, 20]
20	0.28	88.8 ± 36.3	[19]
21	0.28	88.8 ± 36.6	[18]
22	0.28	90.6 ± 37.3	[17]
23	0.30	31.7 ± 6.22	[18]
24	0.35	82.7 ± 8.4	[26]
25	0.3519	83 ± 14	[27]
26	0.352	84.7 ± 14.3	[23]
27	0.38	81.5 ± 1.9	[28]
28	0.3802	83 ± 13.5	[29]
29	0.4	87 ± 17.4	[20]
30	0.4	95 ± 17	[20]
31	0.4004	77 ± 10.2	[29]
32	0.4004	778.6 ± 10.4	[29]
33	0.4247	87.1 ± 11.2	[29]
34	0.4247	88.9 ± 11.4	[29]
35	0.43	86.5 ± 3.7	[25]
36	0.43	88.3 ± 3.8	[17]
•		•	1

Sl No.	Z	$H(z)$ with $\sigma_H(z)$	Ref.
37	0.44	82.6 ± 7.8	[30]
38	0.44	84.3 ± 7.9	[30]
39	0.4497	92.8 ± 12.9	[29]
40	0.4497	94.7 ± 13.1	[29]
41	0.47	89 ± 34	[31]
42	0.47	89 ± 49.6	[24, 31]
43	0.47	90.8 ± 50.6	[31]
44	0.4783	80.9 ± 9	[29]
45	0.4783	82.5 ± 9.2	[31]
46	0.48	97 ± 9	[21]
47	0.48	99 ± 63.2	[32]
48	0.51	90.4 ± 1.9	[28]
49	0.57	92.9 ± 7.855	[33]
50	0.57	96.8 ± 3.4	[33]
51	0.593	104 ± 13	[22]
52	0.593	106.1 ± 13.3	[29]
53	0.6	87.9 ± 6.1	[30]
54	0.6	89.7 ± 6.2	[19]
55	0.61	97.3 ± 2.1	[28]
56	0.6797	92 ± 8	[29]
57	0.68	92 ± 8	[22]
58	0.68	93.9 ± 8.1	[29]
59	0.73	97.3 ± 7	[30]
60	0.73	99.3 ± 7.1	[30]
61	0.781	107.1 ± 12.2	[29]
62	0.782	105 ± 12	[22]
63	0.875	127.6 ± 17.3	[29]
64	0.8754	125 ± 17	[22]
65	0.88	90 ± 40	[21]
66	0.88	91.8 ± 40.8	[32]
67	0.88	117 ± 23.4	[20]
68	0.9	69 ± 12	[20]
69	0.9	117 ± 23	[21]
70	0.9	119.4 ± 23.4	[20]
71	1.037	154 ± 20	[22]
72	1.037	157.2 ± 20.4	[29]

Sl No.	Z	$H(z)$ with $\sigma_H(z)$	Ref
73	1.3	168 ± 17	[21]
74	1.363	160 ± 33.6	[27]
75	1.363	163.3 ± 34.3	[27]
76	1.43	177 ± 18	[21]
77	1.53	140 ± 14	[21, 20]
78	1.53	142.9 ± 14.2	[20]
79	1.75	202 ± 40	[21]

Sl No.	Z	$H(z)$ with $\sigma_H(z)$	Ref.
80	1.75	206.1 ± 40.8	[20]
81	1.965	186.5 ± 50.4	[27]
82	1.965	190.3 ± 51.4	[27]
83	2.3	224.0 ± 8.0	[34]
84	2.34	222 ± 7	[35]
85	2.36	226 ± 8	[36]

4 Constraining Free Parameters of Redshift Parametrization Models using table 1

The chi squared value quantifies the total squared difference between the observed and predicted expansion rates, scaled by observational uncertainty

$$\chi_{OHD}^2(H_0, \ \tilde{\theta}) = \sum_{i=1}^N \frac{\left\{ H_{th} \left(z_i, \tilde{\theta} \right) - H_{obs}(z_i) \right\}^2}{\sigma_z i^2} \quad , \tag{31}$$

where $H_{obs}(z_i)$ is the observed value of the Hubble parameter at redshift (z_i) and $H_{th}\left(z_i, \tilde{\theta}\right)$ is the theoretical value from a model depending on parameters $\tilde{\theta}$ (eg. H_0 , Ω_m , ω_0^{DE} and $\omega_i^{DE'}$ s etc.) $\sigma_{z,i}^2$ denotes the 1σ uncertainty in the observed $H(z_i)$. N is the total count of data points.

Inclusion of the Baryon Acoustic Oscillation (BAO) peak parameter in a cosmological data analysis - especially in combination with H(z) measurements - enhances the constraining power on cosmological parameters. BAO is a "Standard ruler" imprinted in the distribution of galaxies, originally from sound wave in the early universe. A commonly used BAO peak parameter is the volume averaged distance, also called the dilation scale

$$D_v(z) = \left[(1+z)^2 D_A^2(z) \frac{cz}{H(z)} \right]^{\frac{1}{3}}$$

where $D_A(z)$ is the angular diameter distance, c is the speed of light. Another common observable is

$$A(z) = \frac{D_v(z)\sqrt{\Omega_m H_0^2}}{z}$$
 [37]

This is called BAO acoustic parameter, usually measured at specific redshifts,

If we include the BAO acoustic parameter measurement,

$$\chi_{BAO}^2 = \frac{\left[\mathcal{A}_{obs}(z) - \mathcal{A}_{th}(z;\tilde{\theta})\right]^2}{(\sigma_A)^2} \quad , \tag{32}$$

$$\chi_{BAO}^2 = \frac{(\mathcal{A}_{obs}(z) - 0.469)^2}{(0.017)^2} \quad , \tag{33}$$

where we have used the measured value of $\mathcal{A}_{th}(z;\tilde{\theta})$ and σ_A are 0.469 and 0.017 respectively as obtained by [37].

The Cosmic Microwave Background encodes the state of the early universe - particularly the geometry and expansion at the surface of last scattering (redshift $z \approx 1090$). Instead of using the fall CMB power spectrum, which is computationally expensive, we often use a few compressed parameters (like R, l_a , z_A) that capture most of the cosmological information, especially for background dynamics (e.g, H_0 , Ω_m , Ω_k etc.). The shift parameter R which effectively shifts the angular scale of acoustic peaks in the CMB, encapsulating low matter content and geometry affect these positions. This is given as

$$R = \sqrt{\Omega_m H_0^2 \frac{D_A(z_A)}{c}} \quad , \tag{34}$$

where $D_A(z_A)$ is coming angular diameter distance to the last scattering surface, to be measured in a flat universe as

$$D_A(z) = \frac{1}{1+z} \int_0^z \frac{cdz'}{H(z')}$$
 (35)

using Planck 2018 compressed likelihood [38] we obtain $R=1.7492\pm0.0049$ CMB shift parameter is defined as

$$R = \Omega_m^{\frac{1}{2}} \int_0^{z_{ls}} \frac{dz}{E(z)} \quad , \tag{36}$$

where z_{ls} is the redshift at last scattering.

The WMAP7 data gives us $R=1.726\pm0.018$ at z=1091.3 [37, 38, 39, 40, 41, 42]. Chi squared in this case is defined as

$$\chi_{CMB}^2 = \frac{(R - 0.469)^2}{(0.017)^2} \quad . \tag{37}$$

For joint analysis, total chi squared function turns

$$\chi_{tot}^2 = \chi_{OHD}^2 + \chi_{BAO}^2 + \chi_{CMB}^2 \quad . \tag{38}$$

Therefore, the best fit values of different DE model parameters are obtained from Table 1, as we have calculated this particular values in the last column of table 2. Also, different sigma confidence contours are given in fig 1a-1c, 2a-2c, ...11a-c.

Table 2: Different redshift parametrization models with the EoS and best fit values.

Sl. No.	Model	Best fit values of free parameters
1	Linear Redshift parametrisation	$\chi_{CC}^2 = 4600.241321, \omega_0^{LRP} = -0.9985^{+0.1527}_{-0.1397},$
	(LRP) [43]	$\omega_1^{LRP} = -0.9664_{-0.3938}^{+0.4334} ;$
	$\omega^{LRP}(a) = \omega_0^{LRP} + \omega_1^{LRP} \times \left(\frac{1-a}{a}\right)$	$\chi^{2}_{CC+BAO} = 5361.34598, \ \omega^{LRP}_{0} = -0.9934^{+0.1711}_{-0.1684}, \ \omega^{LRP}_{1} = -0.9995^{+0.5419}_{-0.5210} ;$
	$\omega^{LRP}(z) = \omega_0^{LRP} + \omega_1^{LRP} z$	$\chi^{2}_{CC+BAO+CMB} = 14556.024992,$ $\omega^{LRP}_{0} = -0.9900^{+0.1542}_{-0.1516}, \omega^{LRP}_{1} = -0.9960^{+0.4784}_{-0.5038} ;$
2	Chevallier-Polarski-Linder Redshift parametrisation (CPL) [44]	$\chi_{CC}^2 = 4606.814534, \ \omega_0^{CPL} = -0.9983^{+0.2593}_{-0.2647}, \ \omega_1^{CPL} = 0.9960^{+0.8336}_{-0.8338} ;$
	$\omega^{CPL}(a) = \omega_0^{CPL} + \omega_1^{CPL} \times (1 - a)$	$\chi^{2}_{CC+BAO} = 5367.92526, \ \omega^{CPL}_{0} = -0.9935^{+0.2034}_{-0.2083}, \ \omega^{CPL}_{1} = 0.9844^{+0.8762}_{-0.9425} ;$
	$\omega^{CPL}(z) = \omega_0^{CPL} + \omega_1^{CPL} \times \frac{z}{1+z}$	$\chi^{2}_{CC+BAO+CMB} = 14562.604273,$ $\omega^{CPL}_{0} = -0.9930^{+0.2670}_{-0.2672}, \omega^{CPL}_{1} = 1.3007^{+1.2454}_{-1.2234} ;$
3	Jassal-Bagala -Padmanabhan Redshift Parameterization(JBP) [45]	$\chi^2_{CC} = 4611.217324, \ \omega^{JBP}_0 = -0.9935^{+0.2951}_{-0.2854}, \ \omega^{JBP}_1 = -0.9964^{+0.8897}_{-0.8803} ;$
	$\omega^{JBP}(a) = \omega_0^{JBP} + \omega_1^{JBP} \times a(1-a)$	$\chi^{2}_{CC+BAO} = 5372.32805, \ \omega^{JBP}_{0} = -0.9964^{+0.4225}_{-0.3882}, \ \omega^{JBP}_{1} = -1.4092^{+1.0850}_{-1.1413} ;$
	$\omega^{JBP}(z) = \omega_0^{JBP} + \omega_1^{JBP} \times \frac{z}{(1+z)^2}$	$\chi^{2}_{CC+BAO+CMB} = 14562.604273,$ $\omega^{JBP}_{0} = -0.9930^{0.2673}_{-0.2676}, \ \omega^{JBP}_{1} = -1.2124^{1.0046}_{-1.0862} ;$
	Efstathiou Redshift	$\chi_{CC}^2 = 4603.496460, \omega_0^{Log} = -0.9958^{+0.2055}_{-0.2008},$
\parallel 4	Parametrization or, Log Parametrization(ERP)[46]	$\omega_1^{Log} = 0.9986^{+0.7365}_{-0.7090} ;$
	$\omega^{Log}(a) = \omega_0^{Log} + \omega_1^{Log} ln(a)$	$\chi^{2}_{CC+BAO} = 5364.607187, \ \omega^{Log}_{0} = -0.9955^{+0.2382}_{-0.2295}, \ \omega^{Log}_{1} = -0.9977^{+0.7773}_{-0.7577} ;$
	$\omega^{Log}(z) = \omega_0^{Log} + \omega_1^{Log}(1+z)$	$\chi^{2}_{CC+BAO+CMB}, = 14556.513247,$ $\omega^{Log}_{0} = -0.9989^{+0.2769}_{-0.2790}, \omega^{Log}_{1} = -1.0439^{+1.0063}_{-0.8637}$
5	Feng-Shen-Li-Li (FSLL)-I[47]	$\chi_{CC}^2 = 4601.529968,$ $\omega_0 = -0.9922^{+0.4275}_{-0.4123}, \ \omega_1 = -1.0253^{+0.5449}_{-0.5455} ;$
	$\omega^{(FSLL)-I}(a) = \omega_0^{(FSLL)-I} + \omega_1^{(FSLL)-I} \frac{a(1-a)}{1-2a+2a^2}$	$\chi^{2}_{CC+BAO} = 5362.640695,$ $\omega^{(FSLL)-I}_{0} = -0.9958^{+0.4329}_{-0.4186},$ $\omega^{(FSLL)-I}_{1} = -0.9917^{+0.5760}_{-0.5689} ;$
	$\omega_0^{(FSLL)-I}(z) = \omega_0^{(FSLL)-I} + \omega_1^{(FSLL)-I} \frac{z}{1+z^2}$	$\chi^{2}_{CC+BAO+CMB} = 14557.319707,$ $\omega^{(FSLL)-I}_{0} = -0.9988^{+0.4444}_{-0.4367},$ $\omega^{(FSLL)-I}_{1} = -0.9835^{+0.4827}_{-0.4766} ;$
6	Feng-Shen-Li-Li (FSLL)-II[47]	$\chi_{CC}^2 = 4604.279729, \ \omega_0^{(FSLL)-II} = -0.9956^{+0.1676}_{-0.1636}, \ \omega_1^{(FSLL)-II} = -0.9841^{+0.7651}_{-0.7349} ;$

Sl. No.	Model	Best fit values of free parameters
	$\omega^{(FSLL)-II}(a) = \omega_0^{(FSLL)-II} + \omega_1^{(FSLL)-II} \frac{(1-a)^2}{1-2a+2a^2}$	$\chi^2_{CC+BAO} = 5365.390455,$ $\omega^{(FSLL)-II}_0 = -0.9968^{+0.1954}_{-0.2000},$ $\omega^{(FSLL)-II}_1 = -0.9810^{+0.7908}_{-0.7760} ;$
	$\omega_0^{(FSLL)-II}(z) = \omega_0^{(FSLL)-II} + \omega_1^{(FSLL)-II} \frac{z^2}{1+z^2}$	$\chi^{2}_{CC+BAO+CMB} = 14554.246121,$ $\omega^{(FSLL)-II}_{0} = -0.9764^{+0.1539}_{-1.1325},$ $\omega^{(FSLL)-II}_{1} = -1.3440^{+0.9292}_{-0.7758} ;$
7	Polynomial Parameterizations-I[48]	$\chi_{CC}^2 = 4601.719931, \ \omega_0^{PolyI} = -0.9982^{+0.3057}_{-0.3052}, \ \omega_1^{PolyI} = -0.9751^{+0.8289}_{-0.8235} ;$
	$\omega^{PolyI}(a) = -1 + \omega_0^{PolyI} \times (2 - a) + \omega_1^{PolyI}(2 - a)^2 \text{ where}$ $\omega_0^{PolyI} = \frac{1}{4} \left(7 + 16c_1^{PolyI} - 9c_2^{PolyI} \right) \text{ and}$ $\omega_1^{PolyI} = -3c_1^{PolyI} - \frac{3}{4} \left(1 - 3c_2^{PolyI} \right)$	$\chi^2_{CC+BAO} = 5362.830658, \omega_0^{PolyI} = -0.9992^{+0.3072}_{-0.3070}, \omega_1^{PolyI} = -0.9706^{+0.8316}_{-0.8307} ;$
	$\omega^{PolyI}(z) = -1 + \omega_0^{PolyI} \times \left(\frac{1+2z}{1+z}\right) + \omega_1^{PolyI} \left(\frac{1+2z}{1+z}\right)^2$	$\chi_{CC+BAO+CMB}^{2} = 14557.509670,$ $\omega_{0}^{PolyI} = -0.9977^{+0.4096}_{-0.4083},$ $\omega_{1}^{PolyI} = -1.0607^{+0.9476}_{-0.9949} ;$
8	Polynomial Parameterizations-II[48]	$\chi_{CC}^2 = 4618.273761, \ \omega_0^{PolyII} = -0.9966^{+0.1976}_{-0.1877}, \ \omega_1^{PolyII} = -0.9842^{+0.7054}_{-0.6539} \ ;$
	$\omega^{PolyII}(a) = -1 + \omega_0^{PolyII} \times (2 - a) + \omega_1^{PolyII} \times \{(2 - a)^2 - 1\}$ $\text{where } \omega_0^{PolyII} = \frac{1}{11} \times \left(14 + 23c_1^{PolyII} - 9c_2^{PolyII}\right)$ $\text{and } \omega_1^{PolyII} = -\frac{3}{11}c_1^{PolyII} - \left(1 + 4c_1^{PolyII} - 3c_2^{PolyII}\right)$	$\chi^{2}_{CC+BAO} = 5379.384487, \ \omega^{PolyII}_{0} = -0.9917^{+0.1917}_{-0.1789}, \ \omega^{PolyII}_{1} = -1.0972^{+0.7172}_{-0.6996} \ ;$
	$\omega^{PolyII}(z) = -1 + \omega_0^{PolyII} \times \left(\frac{1+2z}{1+z}\right) + \omega_1^{PolyII} \left(\frac{1+2z}{1+z}\right)^2$	$\chi^{2}_{CC+BAO+CMB} = 14561.843239,$ $\omega^{PolyII}_{0} = -0.9985^{+0.1959}_{-0.1723},$ $\omega^{PolyII}_{1} = -1.0269^{+0.6374}_{-0.5076} ;$
9	Barboza-Alcaniz Redshift Parameterization(BA)[49]	$\chi_{CC}^2 = 4601.043255, \omega_0^{BA} = 0.5159_{-0.3478}^{+0.3405}, \\ \omega_1^{BA} = -1.6134_{-0.8508}^{+0.9422} ;$
	$\omega^{BA}(a) = \omega_0 + \omega_1 \frac{1-a}{1-2a+2}$	$\chi^{2}_{CC+BAO} = 5361.559759, \omega^{BA}_{0} = 0.5464^{+0.3930}_{-0.3993}, \omega^{BA}_{1} = -1.5911^{+1.0014}_{-0.9069} ;$
	$\omega^{BA}(z) = \omega_0^{BA} + \omega_1^{BA} \frac{z(1+z)}{1-z^2}$	$\chi^{2}_{CC+BAO+CMB} = 14556.238771,$ $\omega^{BA}_{0} = 0.5416^{+0.3955}_{-0.4021}, \ \omega^{BA}_{1} = -1.5835^{+1.0068}_{-0.9107} ;$

Sl. No.	Model	Best fit values of free parameters
10	Barboza-Alcaniz-Zhu-Silva Redshift Parametrization (BAZS) [50] $\omega^{BAZS}(a) = \omega_0^{BAZS} - \omega_1^{BAZS} \times \frac{a^{\beta}-1}{\beta}$	$\chi^2_{CC} = 4597.511368, \ \omega^{BAZS}_0 = -0.9886^{+0.2116}_{-0.2175}, \ \omega^{BAZS}_1 = -1.4404^{+0.8485}_{-0.7017}, \ \beta = -2.0214^{+1.7242}_{-1.7297} \ ; \ \chi^2_{CC+BAO} = 5367.852295 \ , \ \omega^{BAZS}_0 = -1.0363^{+0.1610}_{-0.1151}, \ \omega^{BAZS}_1 = -0.8284^{+0.7101}_{-0.5537}, \ \beta = 0.9729^{+0.4361}_{-0.4346} \ ; \ \end{cases}$
	$\omega^{BAZS}(z) = \omega_0^{BAZS} - \omega_1^{BAZS} \times \frac{(1+z)^{-\beta} - 1}{\beta}$	$\chi^{2}_{CC+BAO+CMB}, = 14553.312436,$ $\omega^{BAZS}_{0} = -0.9843^{+0.2039}_{-0.2090}, \omega^{BAZS}_{1} = -1.4892^{+0.8194}_{-0.6822},$ $\beta = 1.9201^{+1.7463}_{-1.7542} ;$
11	Alam-Sahni-Saini-Starobinsky Redshift Parameterization(ASSS)[51, 52]	$\chi_{CC}^2 = 4599.380438, A_0 = -0.9813^{+0.4508}_{-0.4489}, A_1 = 1.9055^{+0.8617}_{-0.9650}, A_2 = 1.0684^{+0.4084}_{-0.4119} ;$
	$\omega^{ASSS}(a) = -1 + \frac{1}{3} \times \frac{A_1 a + 2A_2}{(A_0 a^2 + A_1 a + A_2)}$	$ \chi^{2}_{CC+BAO} = 5360.491164, A_{0} = -0.9931^{+0.5175}_{-0.5152}, $ $ A_{1} = 1.8167^{+0.8966}_{-1.0350}, A_{2} = 1.0714^{+0.4075}_{-0.4113} ; $
	$\omega^{ASSS}(z) = -1 + \frac{1+z}{3} \times \frac{\{A_1 + 2A_2(1+z)\}}{(A_0 + A_1(1+z) + A_2(1+z)^2)}$	$\chi^{2}_{CC+BAO+CMB} = 14555.128466,$ $A_{0} = -0.9943^{+0.3754}_{-0.3758}, A_{1} = 2.0541^{+0.8053}_{-0.8428},$ $A_{2} = 1.0704^{+0.4122}_{-0.4142} ;$

In figure 1a to 1c, we have plotted the confidence contours of the free parameters and Gaussian distribution of the each of the parameters ω_0^{LRP} and ω_1^{LRP} for the model table 2-row 1 and data incorporated in table 1. In fig 1a, both the distributions of ω_0^{LRP} and ω_1^{LRP} are positively/right skewed. The probability distributions of both parameters have a longer tail towards higher values. The parameter's most likely (mode) value is lower than its mean. In parameter estimation, this suggests that while smaller values are preferred, the data still allows for a subset of much larger values with non-negligible probability. This supports presence of phantom to be likely. Fig 1b shows approximately symmetric distribution of ω_0^{LRP} . In fig 1c, ω_0^{LRP} is slightly left skewed. If the posterior distribution of the present-day DE EoS parameter w_0 is left-skewed, the most probable values correspond to $w_0 > -1$, representing a quintessence-like behavior of DE. However, the extended tail toward lower values ($w_0 < -1$) implies that a phantom-like regime is statistically allowed, albeit with lower probability. This asymmetry indicates that current observational data primarily favor a mildly dynamical DE model close to the quintessence domain, while still permitting limited phantom crossing within the uncertainty bounds.

Figure 2a-c are free parameter contraining plots for CPL model. Here, both ω_0^{CPL} and ω_1^{CPL} are followed to be left skewed. The the latter tilts more. A left-skewed posterior implies that larger values of the parameter are more probable, while there exists a non-negligible tail extending toward smaller values. In such a distribution, the most likely value (mode) lies above the mean, indicating that the lower parameter regime is less favored but remains statistically allowed. Cosmologically interpreting, phantom era is not likely with this model. Quintessence gets a good cheer up by the distribution of free parameters.

In figure 3a-c, we have plotted different confidence contours of ω_0^{JBP} and ω_1^{JBP} . Nature of free parameters' distribution match those of the CPL case. Only, H(z) - z + BAO case evolves a convolution of two distributions. If the two component means differ significantly, then the two peaks remain distinct, producing a bimodal posterior. Here, two distinct physical regimes may become comparably probable. In a

Fig. 1(a): For H(z)-z data Analysis

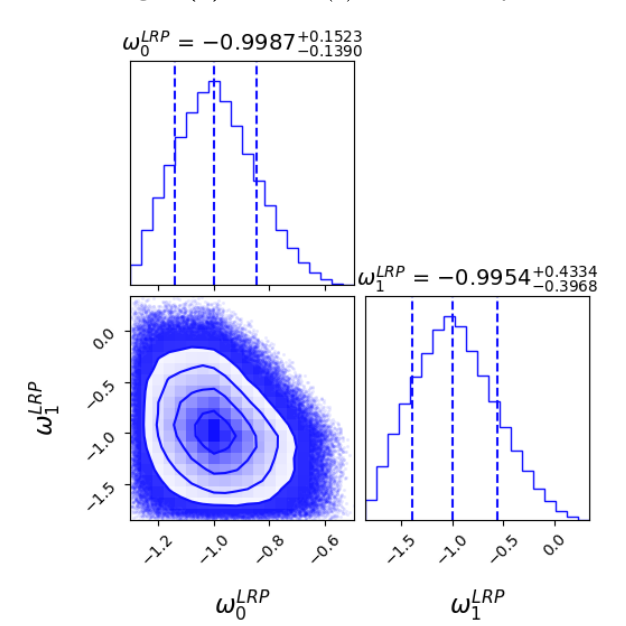


Fig. 1(c): For H(z)-z+BAO+CMB Analysis

Fig. 1(b): For H(z)-z+BAO Analysis

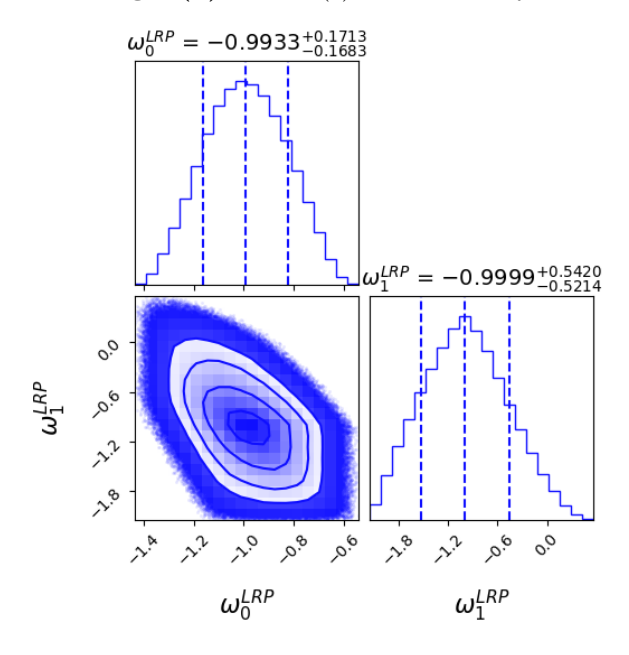
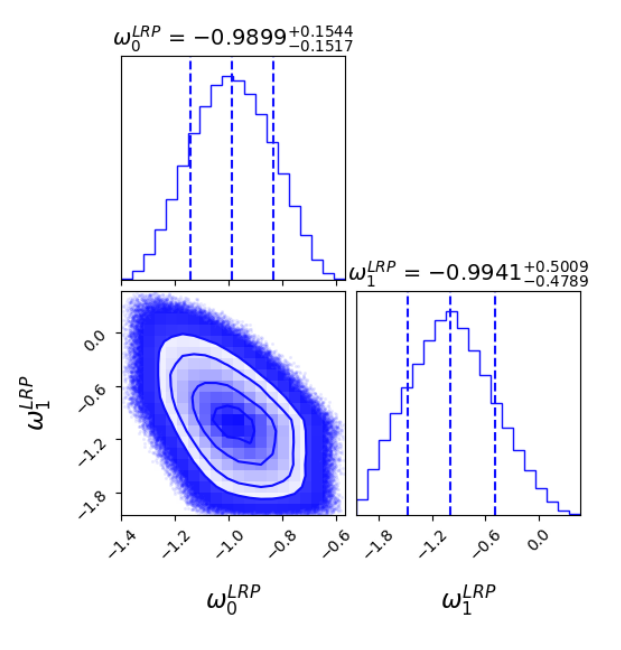


Fig. 1(d): $\log(\frac{M}{M_0})$ vs redshift plot



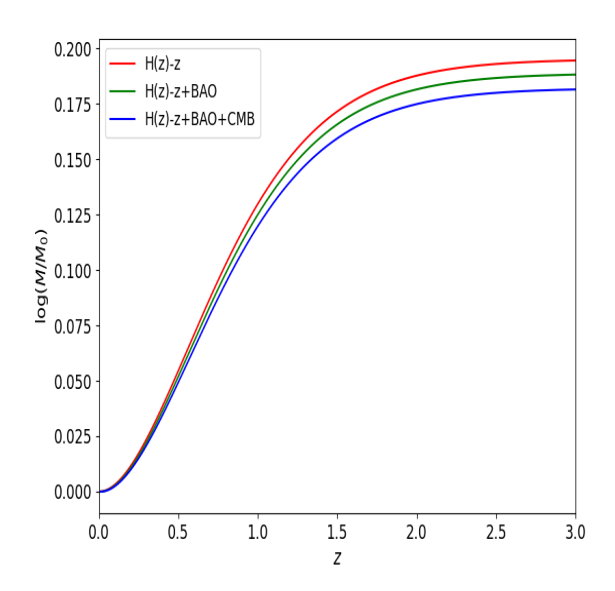
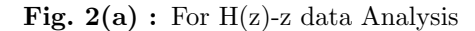


Figure 1: Fig. 1(a-c) represents confidence contours in $\omega_0^{LRP} - \omega_1^{LRP}$ plane and individual distributions of free parameters ω_0^{LRP} and ω_1^{LRP} . 1(d) represents the variation of the log $\left\{\frac{M}{M_0}\right\}$ due to the accretion of LRP type DE onto a MCG contaminated BH.

cosmological context, this situation can occur when the data admit two equally good fits - one corresponding to the Λ CDM limit ($w_0 \approx -1$) and another lying in the phantom regime ($w_0 < -1$). Such a scenario signals a degeneracy in the parameter space, where the likelihood surface develops two nearly equivalent maxima.

In figure 4a-c, we will plot the distribution and confidence contours of Efststathuou redshift parametrization model's free parameters. Hubble data and BAO constrain are found to constrain the free parameters



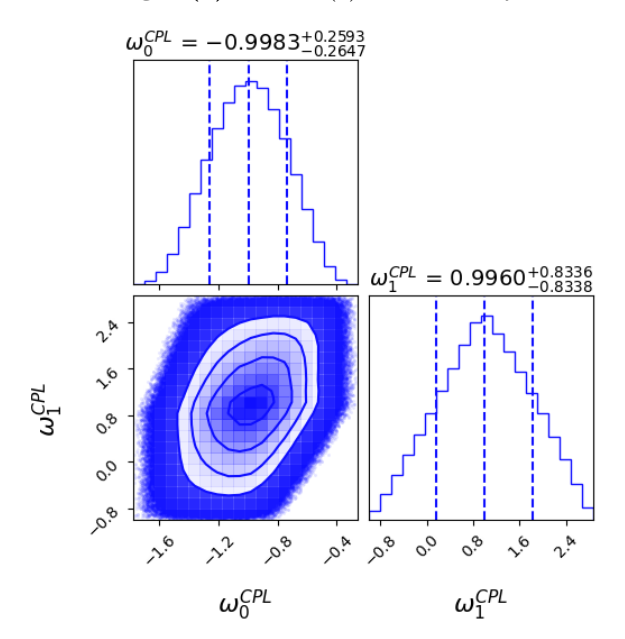
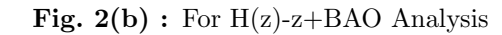


Fig. 2(c): For H(z)-z+BAO+CMB Analysis



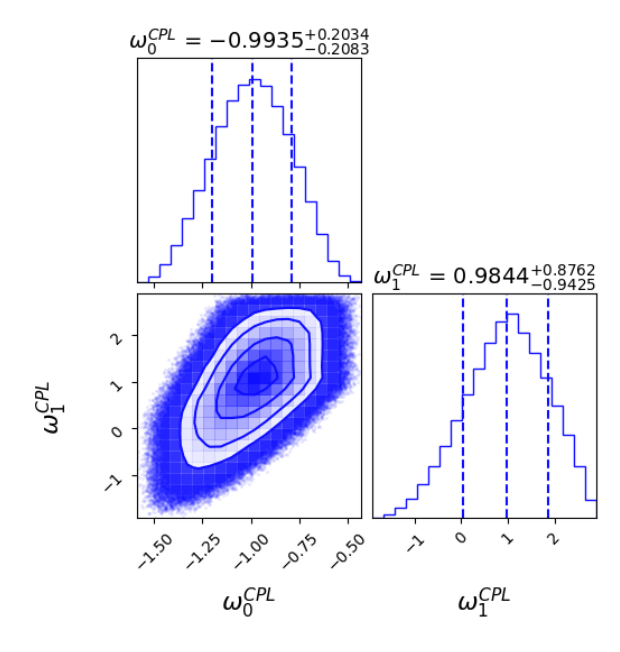
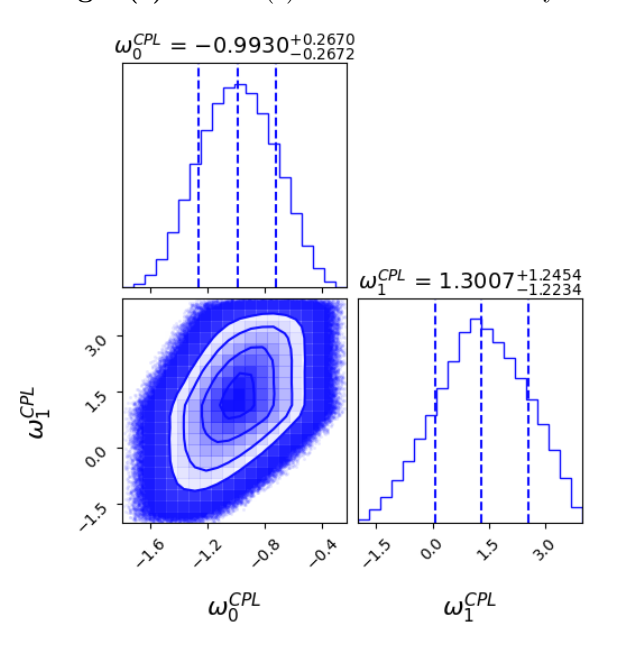


Fig. 2(d): $\log(\frac{M}{M_0})$ vs redshift plot



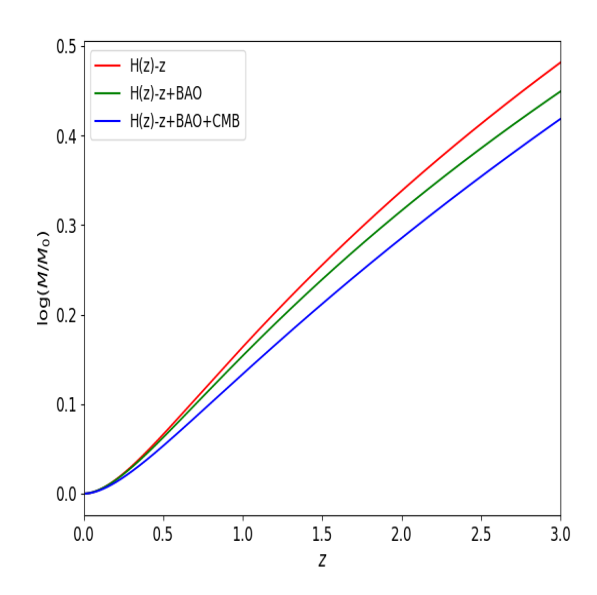
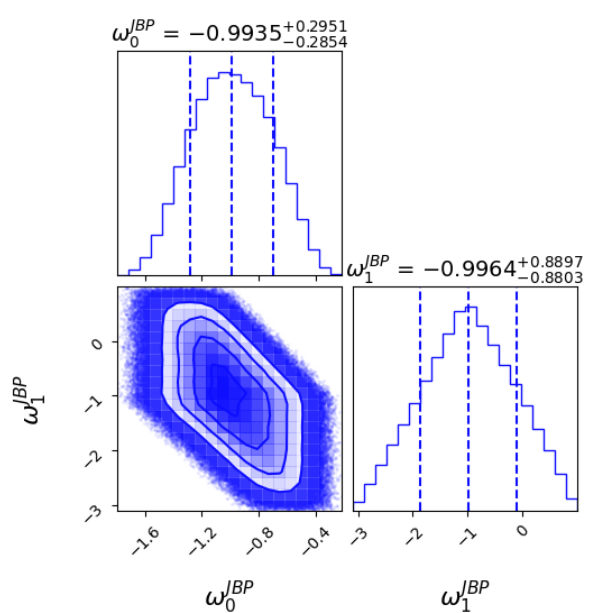
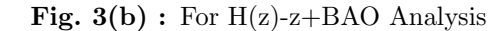


Figure 2: Fig. 1(a-c) represents confidence contours in $\omega_0^{CPL} - \omega_1^{CPL}$ plane and individual distributions of free parameters ω_0^{CPL} and ω_1^{CPL} . 1(d) represents the variation of the log $\left\{\frac{M}{M_0}\right\}$ due to the accretion of CPL type DE onto a onto a MCG contaminated BH.

almost symmetrically. Only CMB added, the symmetric distribution of ω_1^{ERP} does not follow and turns extremely right skewed. An extremely right-skewed posterior distribution indicates that the most probable values of the parameter lie near the lower bound of its domain, while a long tail extends toward higher values. In the context of dark energy models, this behavior implies that the data strongly favor a small or nearly vanishing deviation from the Λ CDM limit, yet allow the possibility of larger parameter values with pro-

Fig. 3(a): For H(z)-z data Analysis





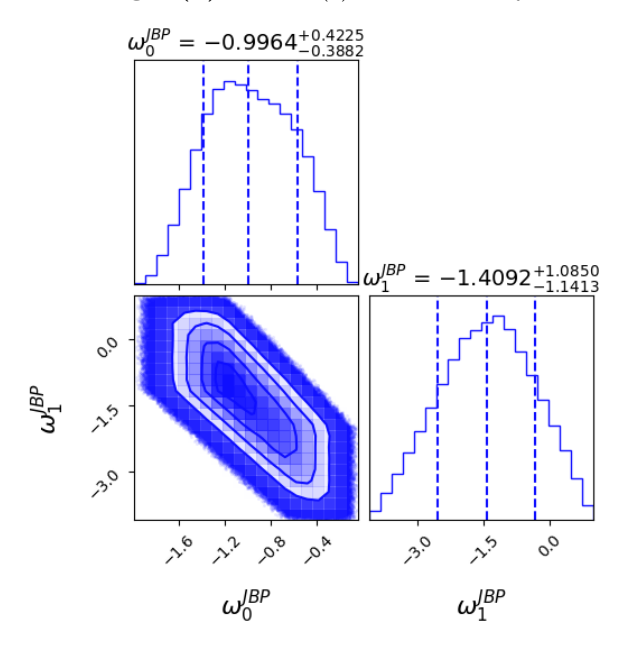
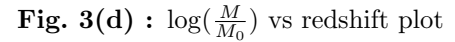
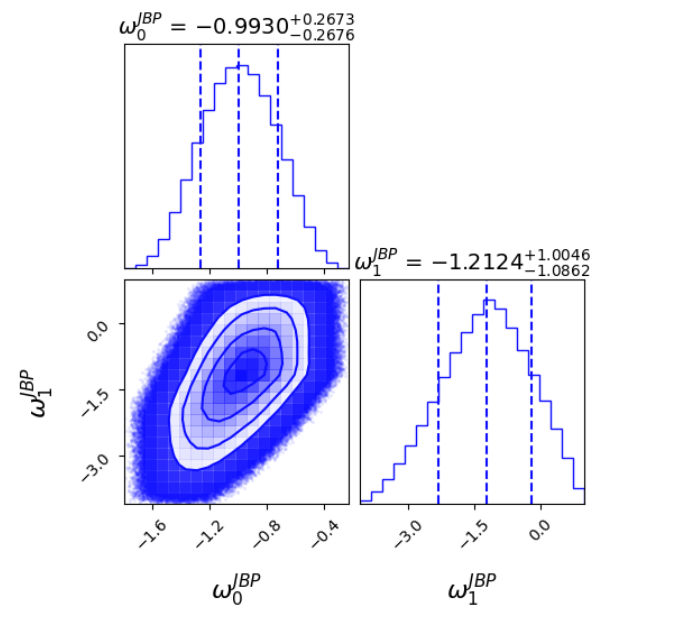


Fig. 3(c): For H(z)-z+BAO+CMB Analysis





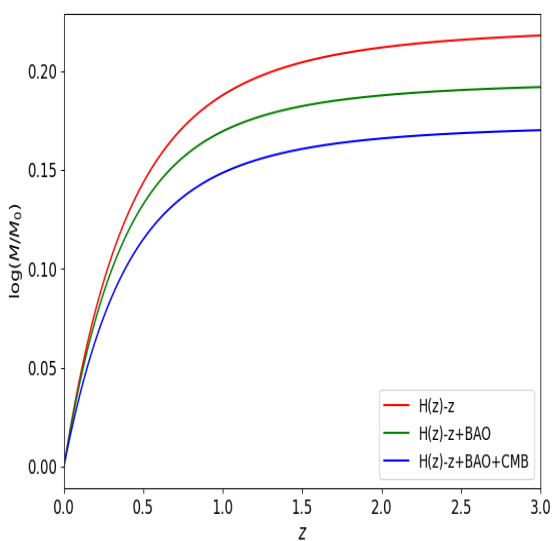


Figure 3: Fig. 1(a-c) represents confidence contours in $\omega_0^{JBP}-\omega_1^{JBP}$ plane and individual distributions of free parameters ω_0^{JBP} and ω_1^{JBP} . 1(d) represents the variation of the log $\left\{\frac{M}{M_0}\right\}$ due to the accretion of JBP type DE onto a MCG contaminated BH.

gressively lower probability. Such asymmetry often arises from one-sided priors, nonlinear model responses, or the degeneracy of cosmological observables at large parameter magnitudes, reflecting a preference for minimal modification with an extended allowance for more exotic regimes.

FSLL-I and FSLL-II models give more or less symmetric distributions which are noted in the figures 5a-c and 6a-c. However, only for OHD+BAO+CMB, both $\omega_0^{FSLL-II}$ and $\omega_0^{FSLL-II}$ are found to be extremely

Fig. 4(a): For H(z)-z data Analysis

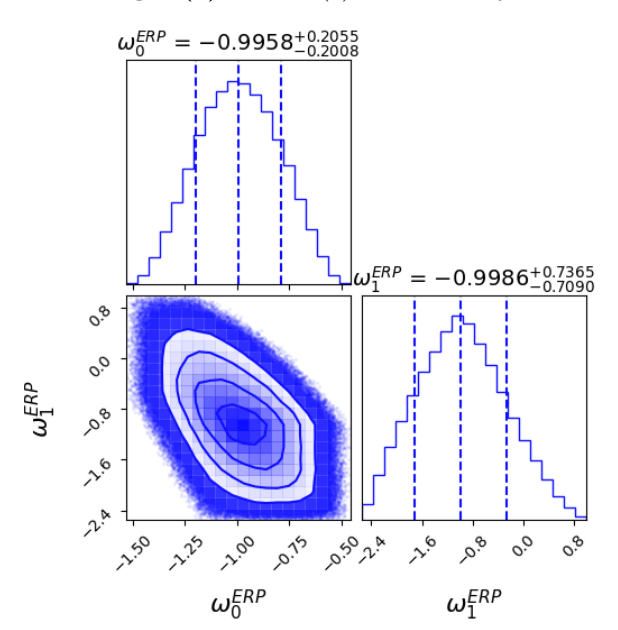
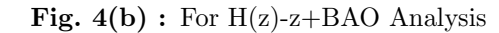


Fig. 4(c): For H(z)-z+BAO+CMB Analysis



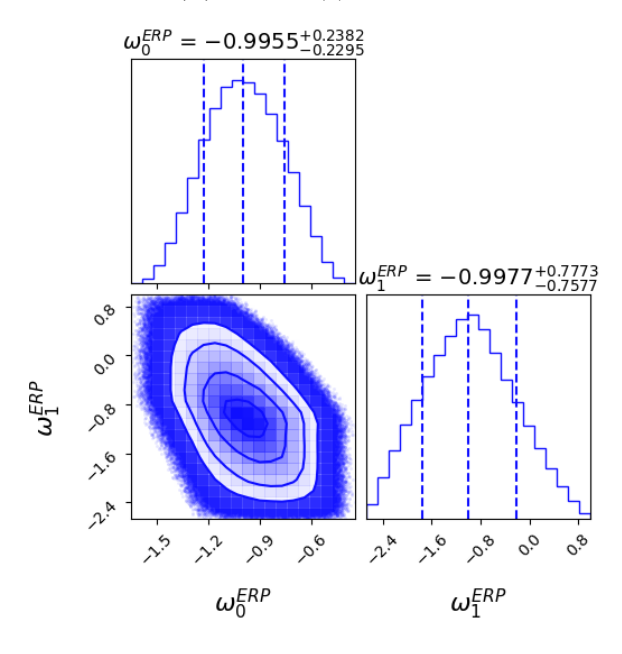
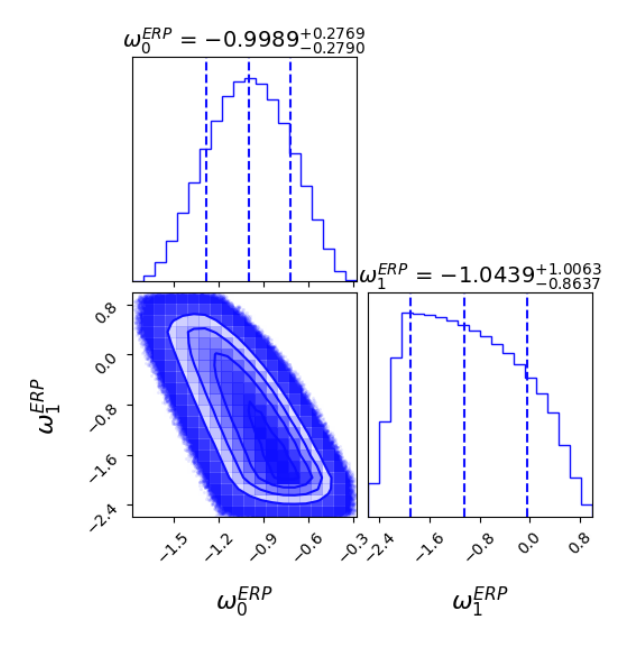


Fig. 4(d): $\log(\frac{M}{M_0})$ vs redshift plot



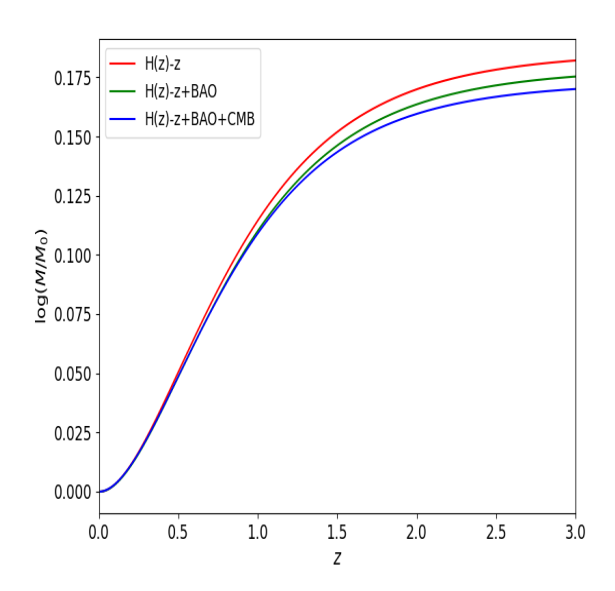
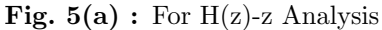
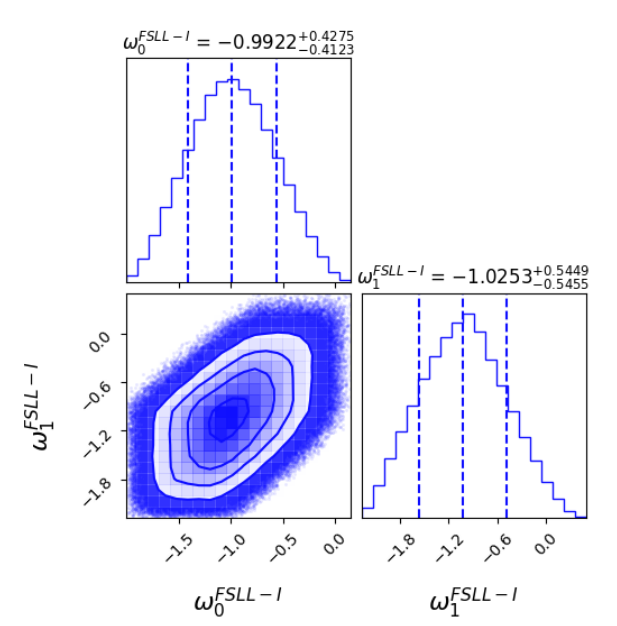


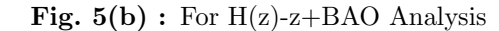
Figure 4: Fig. 1(a-c) represents confidence contours in $\omega_0^{ERP} - \omega_1^{ERP}$ plane and individual distributions of free parameters ω_0^{ERP} and ω_1^{ERP} . 1(d) represents the variation of the log $\left\{\frac{M}{M_0}\right\}$ due to the accretion of ERP type DE onto a MCG contaminated BH.

right skewed.

In the figure 7a-c and 8a-c, we keep the distributions of free parameters of Ploy nomial-I and Polynomial II redshift models respectively. Symmetricity around the respective means are found in ply-I case. Left skewness enters when poly-Ii is fitted with H(z) - z + BAO + CMB. In figure 9a-c, where we have plotted the distributions and confidence contours for Barboza Alcaniz model. ω_0^{BA} stays symmetric around the mean.







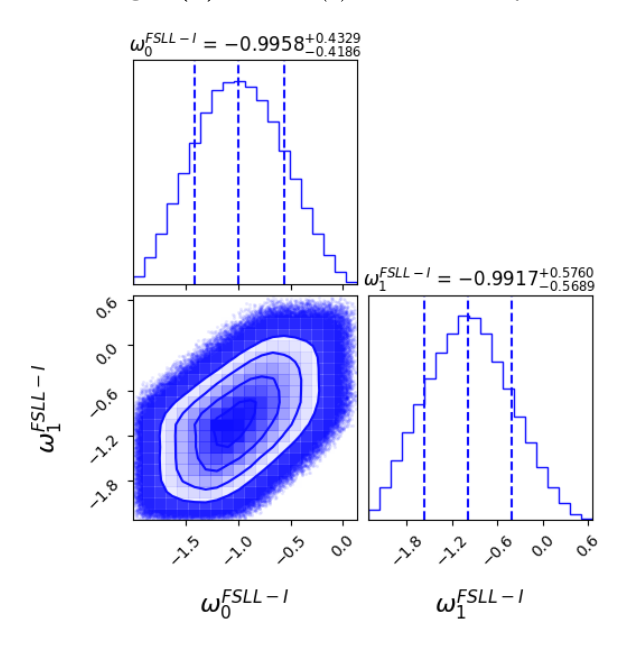
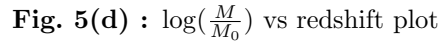


Fig. 5(c): For H(z)-z+BAO+CMB Analysis



3.0

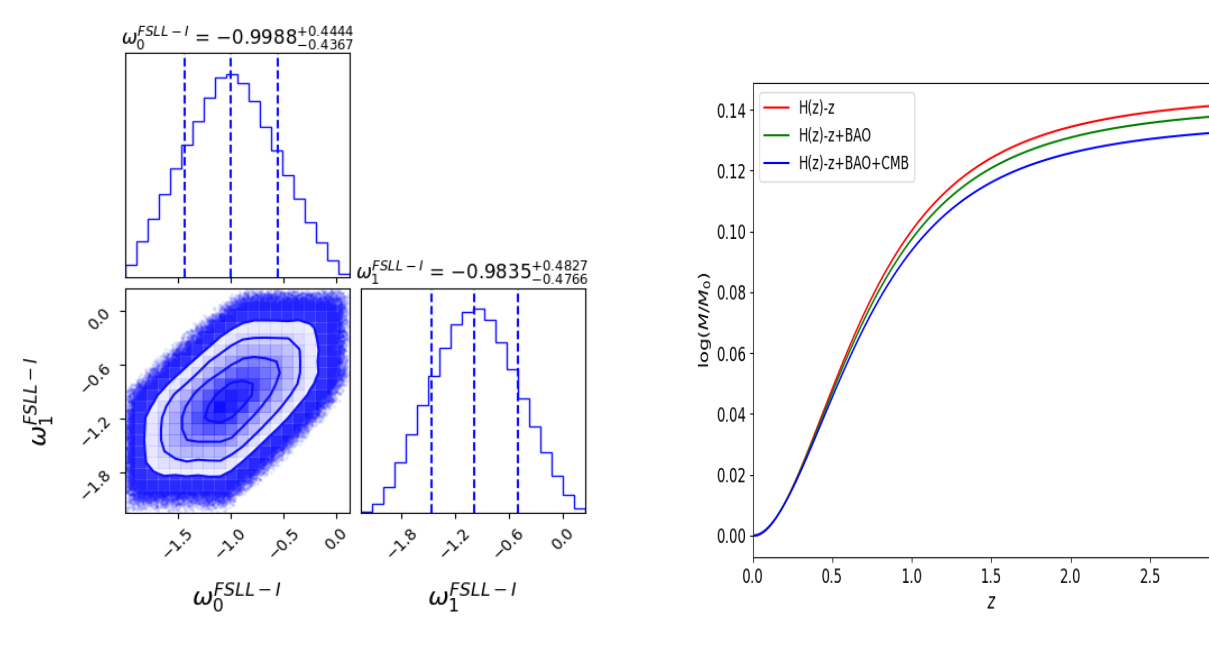
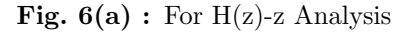


Figure 5: Fig. 1(a-c) represents confidence contours in $\omega_0^{FSLL-I} - \omega_1^{FSLL-I}$ plane and individual distributions of free parameters ω_0^{FSLL-I} and ω_1^{FSLL-I} . 1(d) represents the variation of the log $\left\{\frac{M}{M_0}\right\}$ due to the accretion of FSLL-I type DE onto a MCG contaminated BH.

But ω_1^{BA} is found to act slightly left skewed. A left-skewed posterior for ω_1 indicates that the most probable dynamics correspond to a mild or positive evolution of $\omega(z)$ with redshift, implying a quintessence-like dark energy component that becomes slightly less negative in the past. The long tail toward negative ω_1 values, although statistically suppressed, represents the phantom branch where the dark energy pressure grows more negative with time, potentially leading to unstable or super-accelerating expansion. The asymmetry



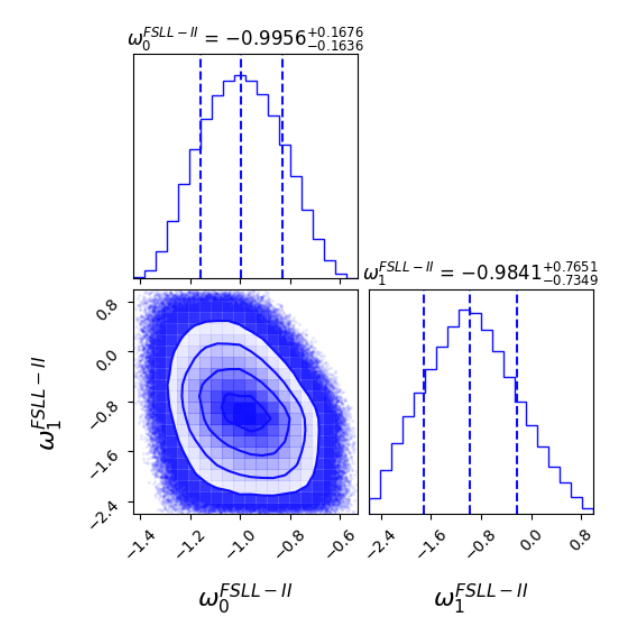
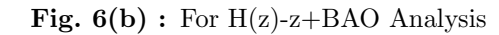


Fig. 6(c): For H(z)-z+BAO+CMB Analysis



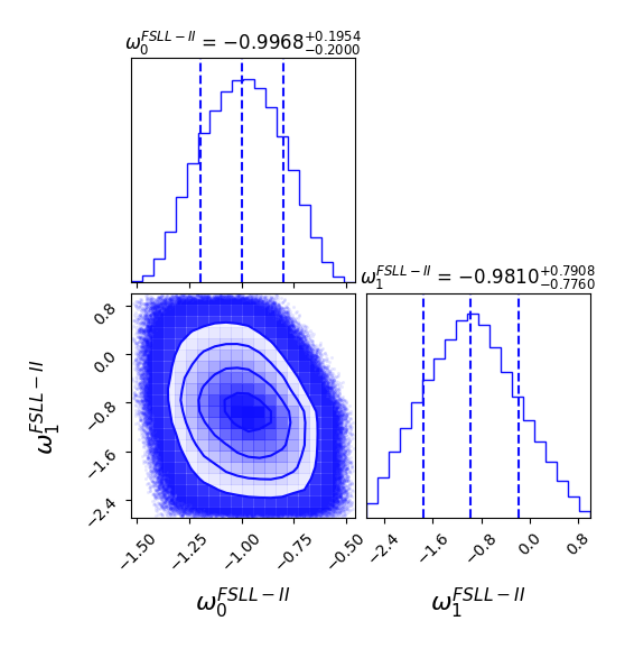
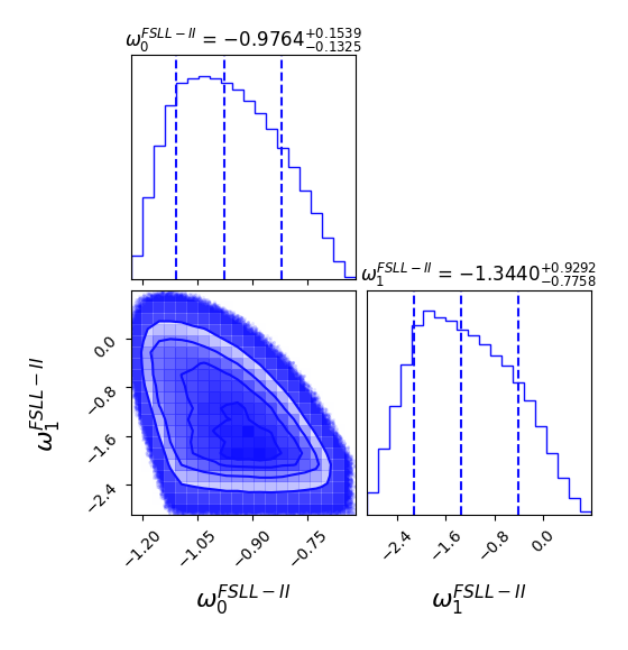


Fig. 6(d): $\log(\frac{M}{M_0})$ vs redshift plot



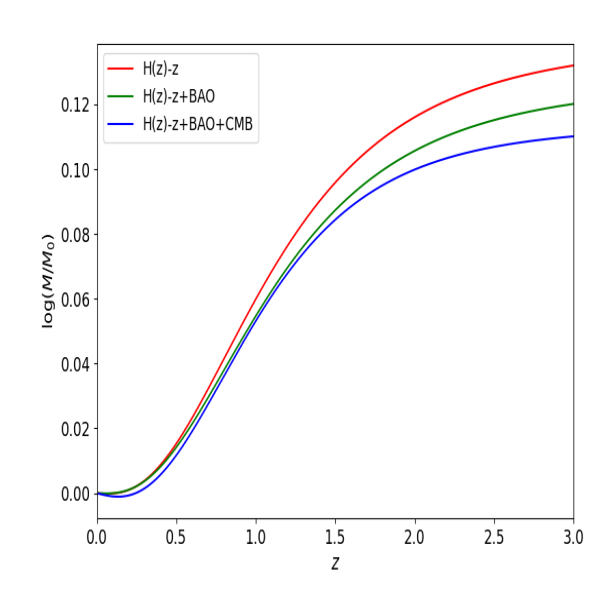
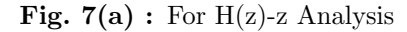


Figure 6: Fig. 1(a-c) represents confidence contours in $\omega_0^{FSLL-II} - \omega_1^{FSLL-II}$ plane and individual distributions of free parameters $\omega_0^{FSLL-II}$ and $\omega_1^{FSLL-II}$. 1(d) represents the variation of the log $\left\{\frac{M}{M_0}\right\}$ due to the accretion of FSLL-II type DE onto a MCG contaminated BH.

arises because the function $z(1+z)/(1+z^2)$ saturates at high redshift, making the expansion history more sensitive to negative than positive variations of ω_1 . Consequently, the Universe dynamically prefers a stable, slowly evolving dark energy field close to the Λ CDM regime, while allowing a faint probability for strongly phantom-like deviations within the tail of the distribution. In figure 10a-c, the distribution and confidences of free parameters of BAZS model are incorporated. Symmetricity mainly is broken for ω_1^{BAZS} . Right



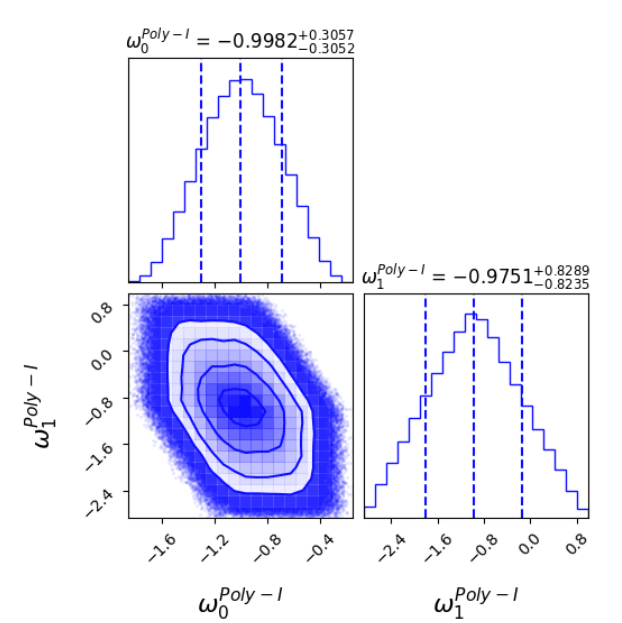
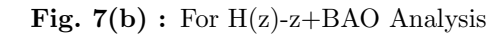


Fig. 7(c): For H(z)-z+BAO+CMB Analysis



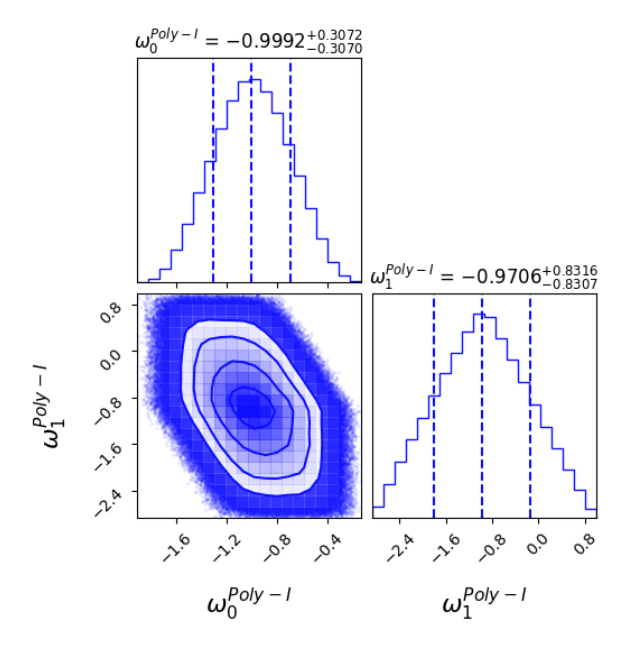
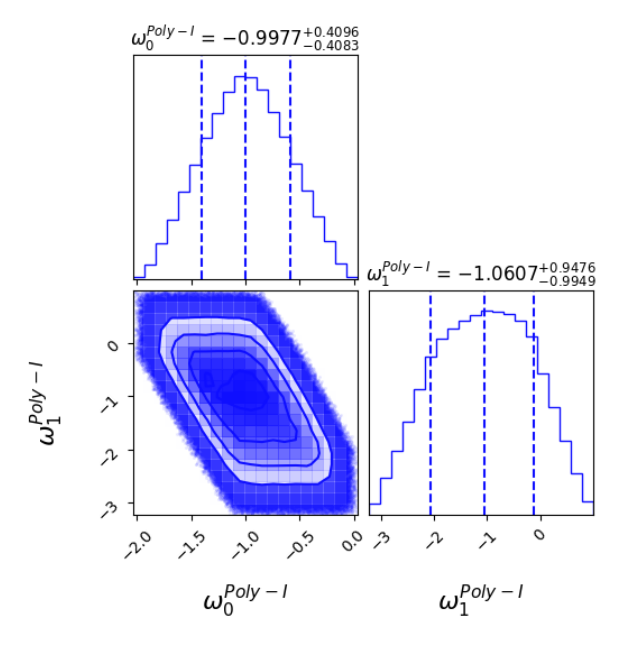


Fig. 7(d) : $\log(\frac{M}{M_0})$ vs redshift plot



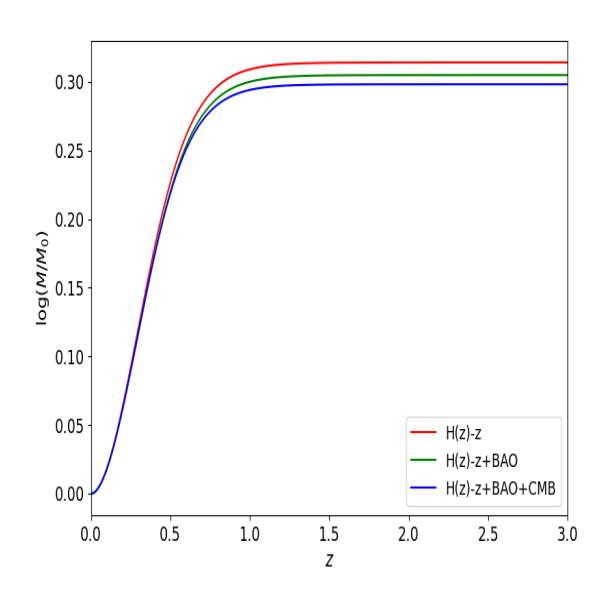


Figure 7: Fig. 1(a-c) represents confidence contours in $\omega_0 - \omega_1$ plane for Polynomial Redshift Parametrisation-I and individual distributions of free parameters ω_0 and ω_1 for Polynomial Redshift Parametrisation-I. 1(d) represents the variation of the log $\left\{\frac{M}{M_0}\right\}$ due to the accretion of Polynomial Redshift Parametrisation-I type DE onto a MCG contaminated BH.

skewness is followed for ω_1^{BAZS} .

Distributions and confidence contours of AAAS model are plotted in figure 11a-c. The parameter A_2^{AAAS} is found to possess leftly skewed distribution.

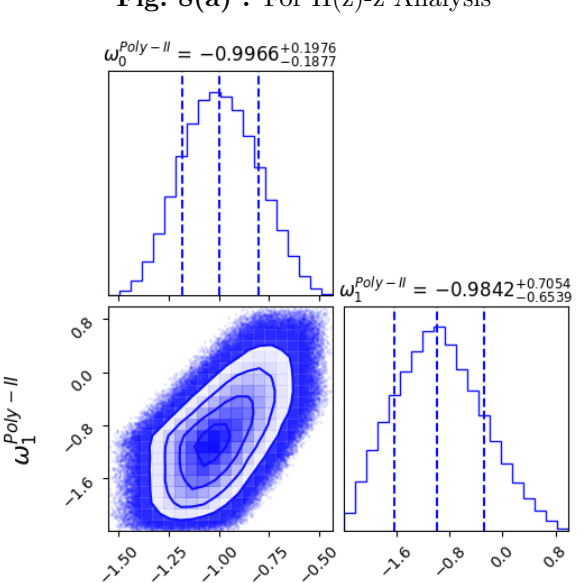


Fig. 8(a): For H(z)-z Analysis

Fig. 8(b): For H(z)-z+BAO Analysis

 $\omega_1^{Poly-II}$

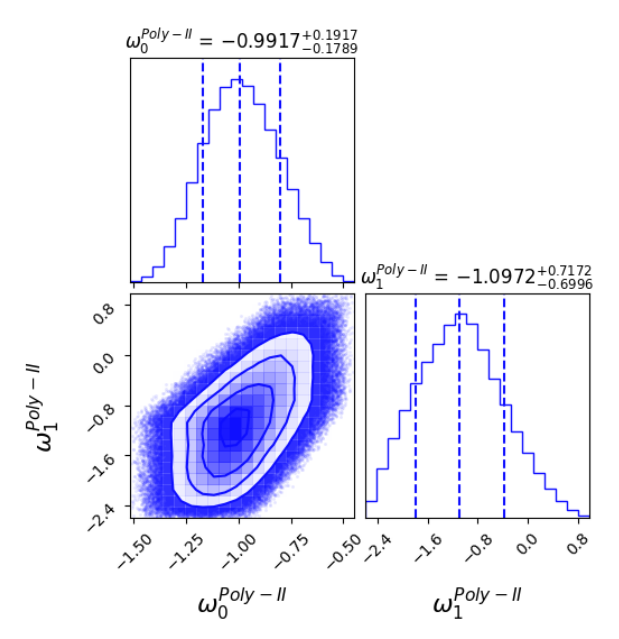


Fig. 8(c): For H(z)-z+BAO+CMB Analysis

 ω_0^{Poly}

Fig. 8(d) : $\log(\frac{M}{M_0})$ vs redshift plot

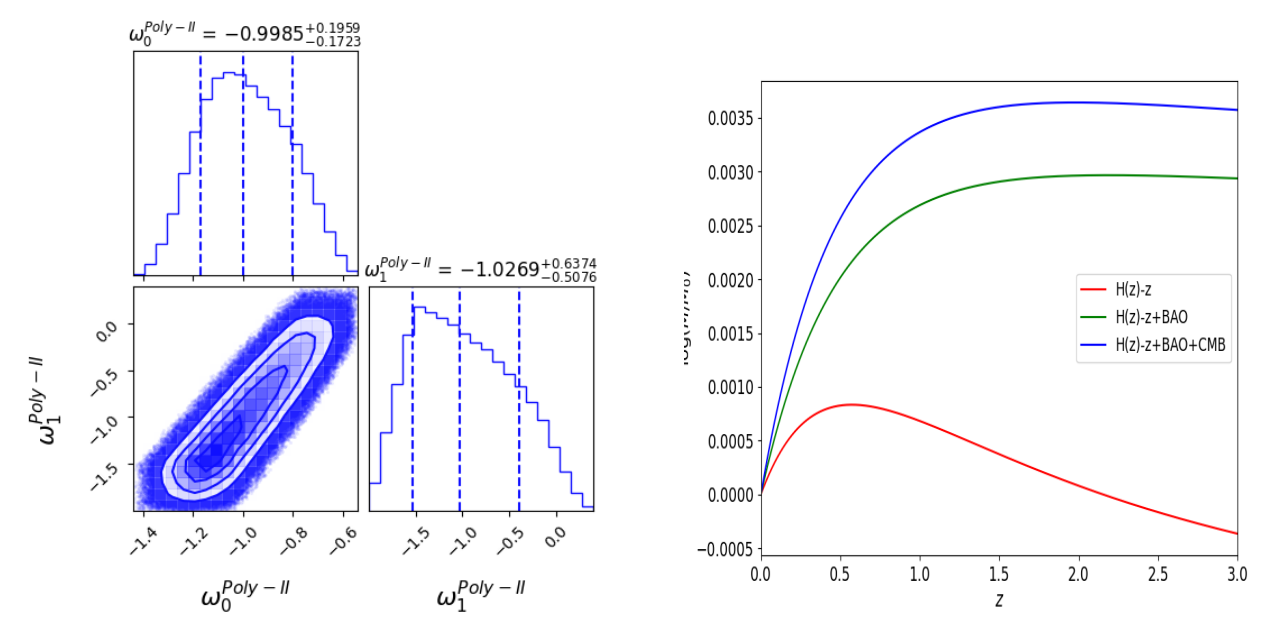


Figure 8: Fig. 1(a-c) represents confidence contours in $\omega_0 - \omega_1$ plane for Polynomial Redshift Parametrisation-II and individual distributions of free parameters ω_0 and ω_1 for Polynomial Redshift Parametrisation-II. 1(d) represents the variation of the log $\left\{\frac{M}{M_0}\right\}$ due to the accretion of Polynomial Redshift Parametrisation-II type DE onto a MCG contaminated BH.

5 Dark Energy Accretion towards Black Holes

Let $u^{\mu} \equiv \frac{dx^{\mu}}{d\tau}$ be the four speed for the μ -th coordinate x^{μ} and τ is the proper time. Using the dot product property of four vectors $u_{\mu}u^{\mu} = 1$. In addition, DE accretion is supposed not to shed any influence on the

Fig. 9(a): For H(z)-z Analysis

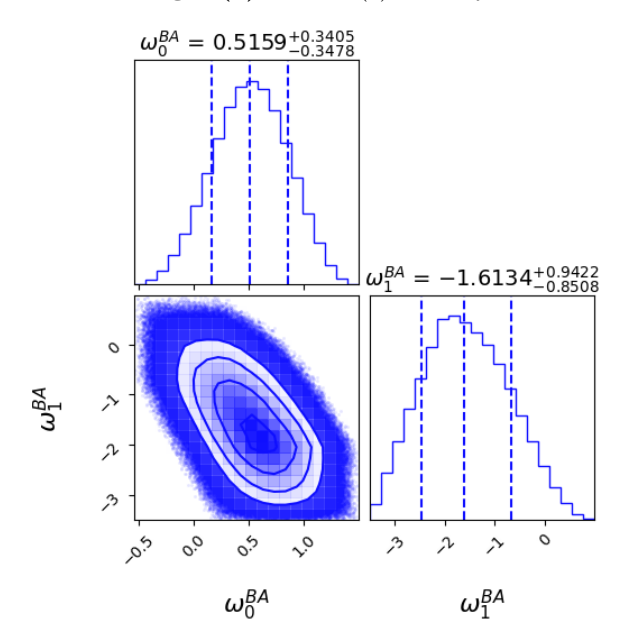


Fig. 9(c): For H(z)-z+BAO+CMB Analysis

Fig. 9(b): For H(z)-z+BAO Analysis

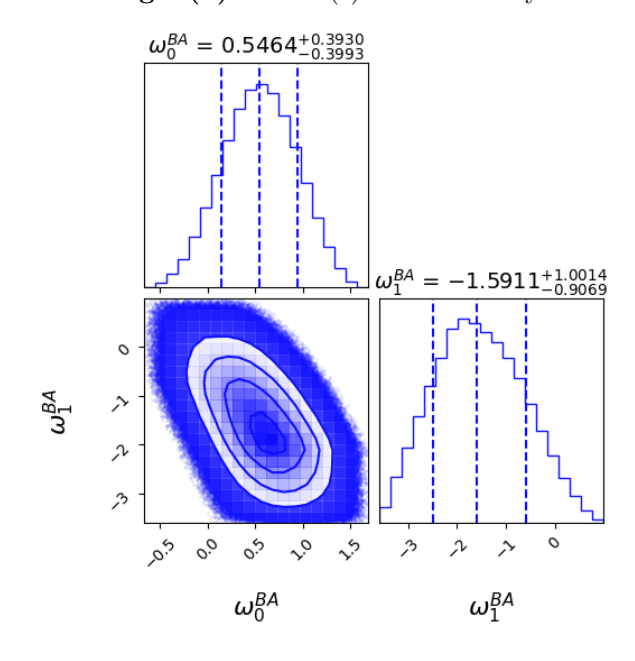
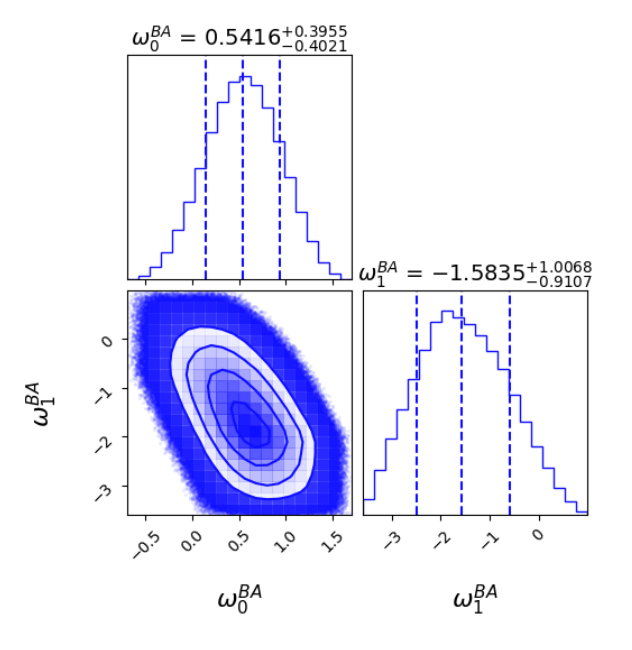


Fig. 9(d): $\log(\frac{M}{M_0})$ vs redshift plot



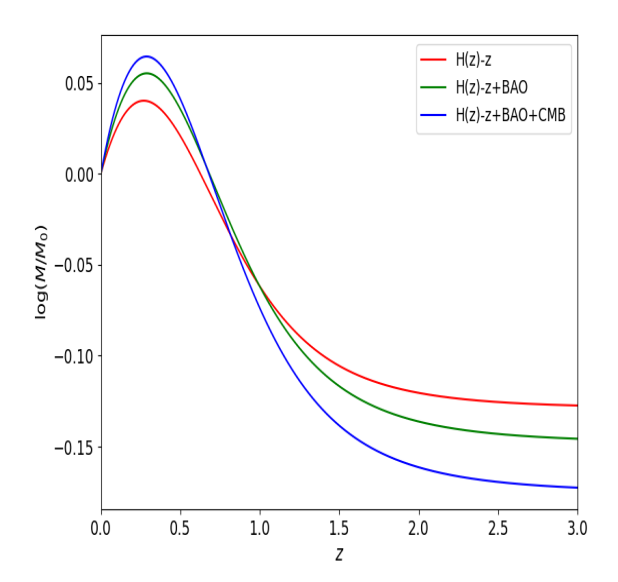
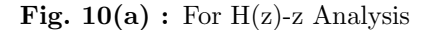


Figure 9: Fig. 1(a-c) represents confidence contours in $\omega_0^{BA} - \omega_1^{BA}$ and individual distributions of free parameters ω_0^{BA} and ω_1^{BA} . 1(d) represents the variation of the log $\left\{\frac{M}{M_0}\right\}$ due to the accretion of BA type DE onto a MCG contaminated BH.

corresponding BH's spherical symmetry. This makes u^{θ} and u^{ϕ} to vanish. For simplicity, $u^{r}=u<0$ (due to infall) is chosen and hence the non zero velocity terms can be written as

$$u_r = g_{rr}u^r = \frac{u}{f_{MCG}(r)}, \quad u^t = \frac{\sqrt{f_{MCG}(r) + u^2}}{f_{MCG}(r)} = \sqrt{\frac{1}{f_{MCG}(r)} + \frac{u^2}{\{f_{MCG}(r)\}^2}} \quad \text{and} \quad u_t = -\sqrt{f_{MCG}(r) + u^2} .$$
(39)



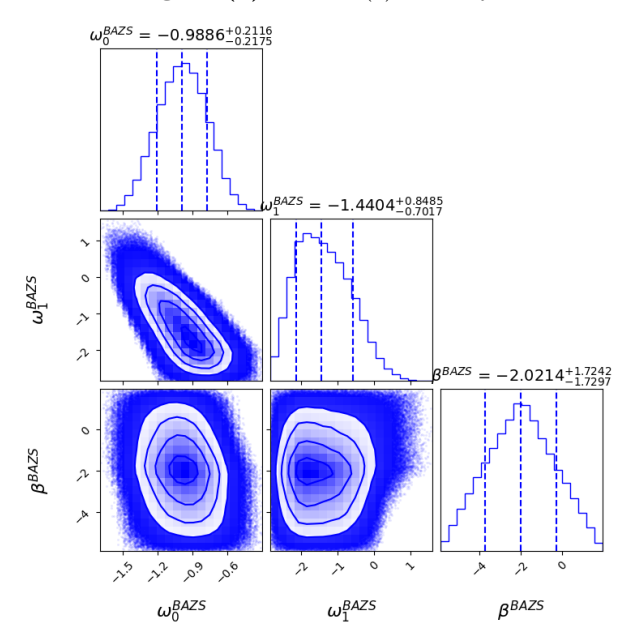


Fig. 10(b): For H(z)-z+BAO Analysis

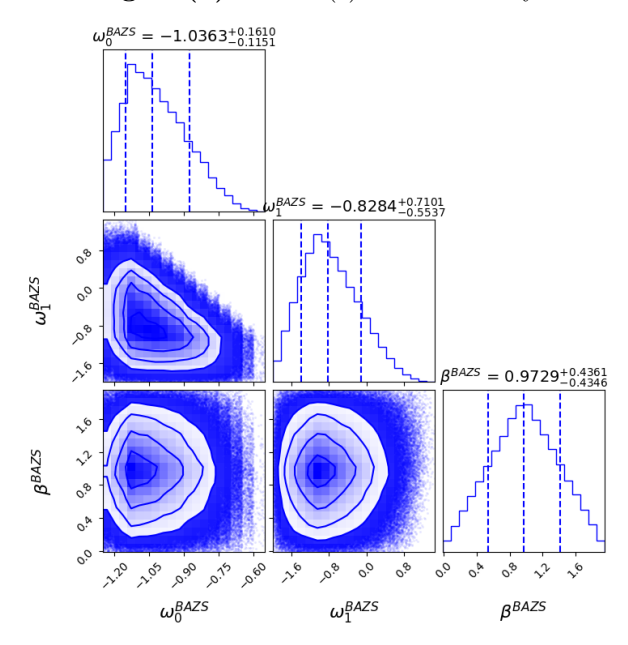
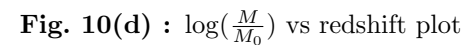
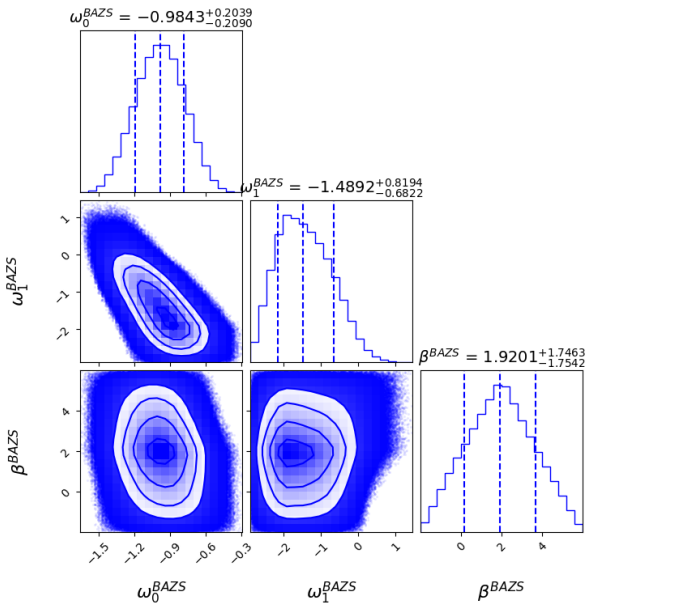


Fig. 10(c): For H(z)-z+BAO+CMB Analysis





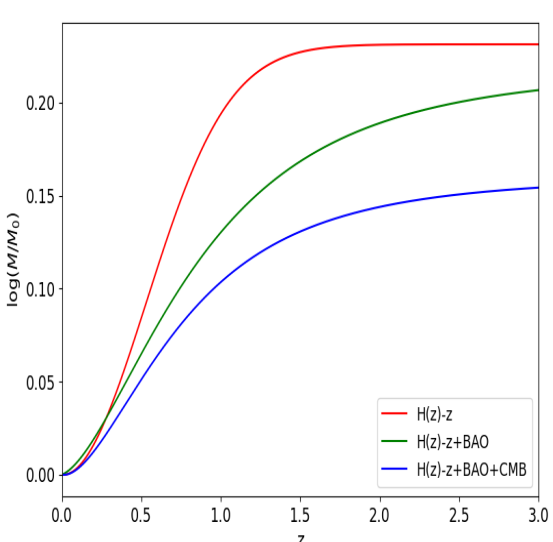


Figure 10: Fig. 1(a-c) represents confidence contours in $\omega_0^{BAZS} - \omega_1^{BAZS}$ and individual distributions of free parameters ω_0^{BAZS} and ω_1^{BAZS} . 1(d) represents the variation of the log $\left\{\frac{M}{M_0}\right\}$ due to the accretion of BAZS type DE onto a MCG contaminated BH.

With these, we construct the components of the stress energy tensor as.

$$T_{t}^{t} = (\rho + p)u^{t}u_{t} + p = -\rho - \frac{u^{2}}{f_{MCG}(r)}(\rho + p) ,$$

$$T_{r}^{r} = (\rho + p)u^{r}u_{r} + p = (\rho + p)\frac{u^{2}}{f_{MCG}(r)} + p ,$$

$$T_{\theta}^{\theta} = T_{\phi}^{\phi} = p \text{ and } T_{t}^{r} = -u(\rho + p)\sqrt{f_{MCG}(r) + u^{2}} .$$

$$(40)$$

Fig. 11(a): For H(z)-z Analysis

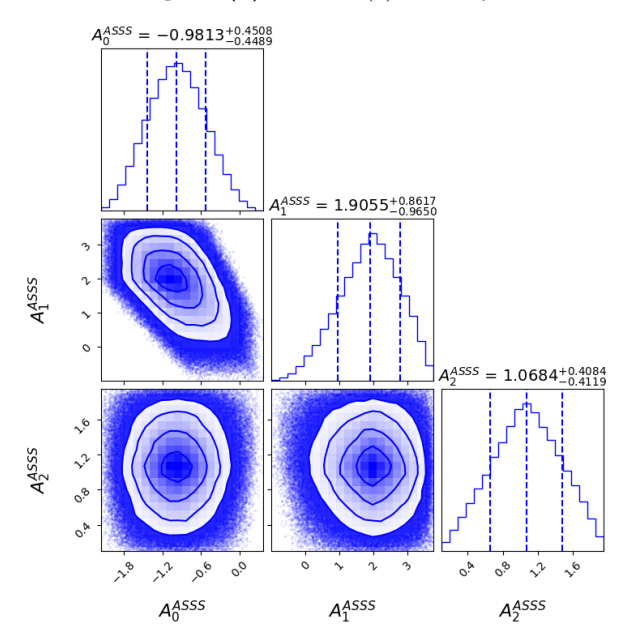
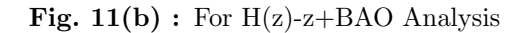


Fig. 11(c): For H(z)-z+BAO+CMB Analysis



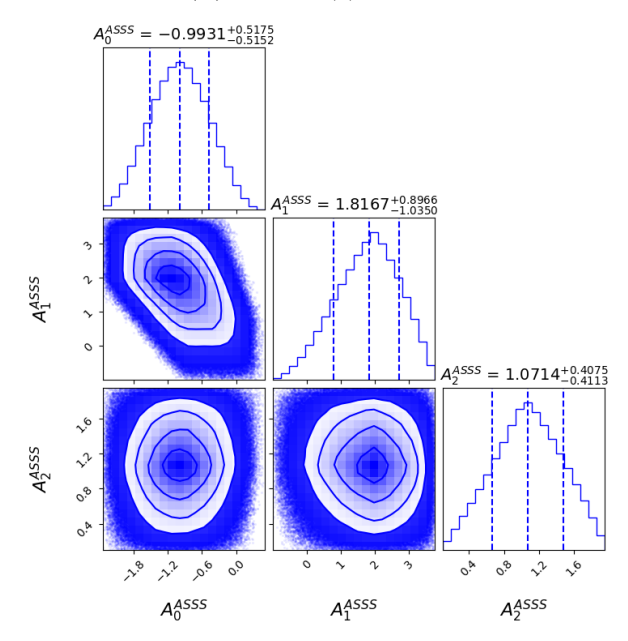
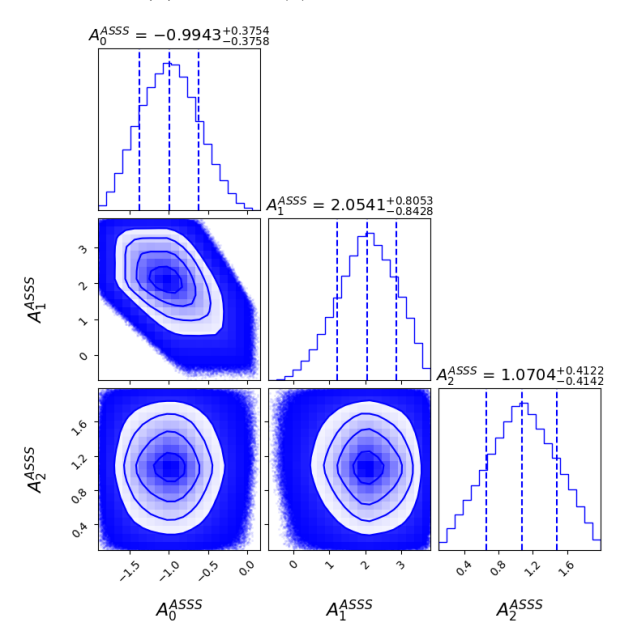


Fig. 11(d): $\log(\frac{M}{M_0})$ vs redshift plot



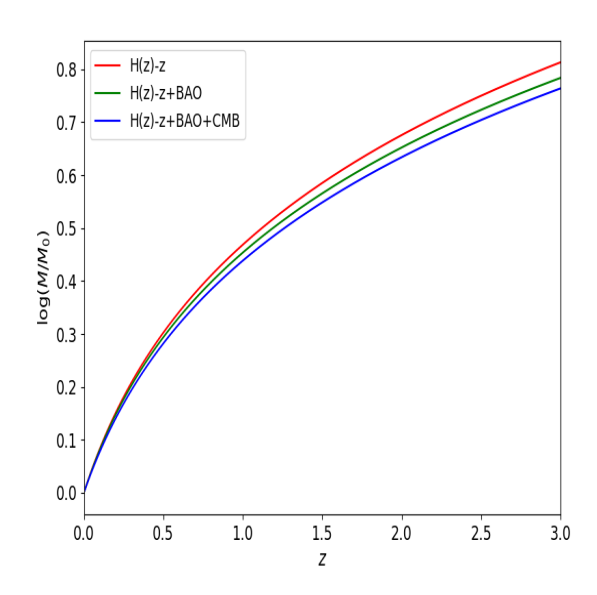


Figure 11: Fig. 1(a-c) represents confidence contours in $\omega_0^{ASSS} - \omega_1^{ASSS}$ and individual distributions of free parameters ω_0^{ASSS} and ω_1^{ASSS} . 1(d) represents the variation of the log $\left\{\frac{M}{M_0}\right\}$ due to the accretion of ASSS type DE onto a MCG contaminated BH.

Along with the 4-current conservation of mass flux, $\frac{\partial J^{\mu}}{\partial x^{\mu}} = 0$ will be simplified now.

$$J^{\mu} = \rho \frac{dx^{\mu}}{d\tau} = \rho \begin{pmatrix} c \\ \frac{dx^{i}}{d\tau} \end{pmatrix} = \begin{pmatrix} c \\ u \\ 0 \\ 0 \end{pmatrix} \quad \Rightarrow \quad \rho u r^{2} = \xi_{0} , \quad \text{a constant} \quad \mu = t, \ r, \ \theta, \ \phi ; \quad i = r, \ \theta, \ \phi . \tag{41}$$

Now we will only opt the t-th component of $T_{\mu;\nu} = 0$ (';' signifies covariant differentiation) i.e., $T^{\nu}_{t;\nu} = 0$, and we obtain

$$0 = T_{t;\nu}^{\nu} = T_{t;t}^{t} + T_{t;r}^{r} + T_{t;\theta}^{\theta} + T_{t;\phi}^{\phi}$$

$$\tag{42}$$

$$\Rightarrow ur^2(\rho+p)\sqrt{f_{MCG}(r)+u^2}M^{-2}=\xi_1$$
, another constant of integration . (43)

(44)

We require another equation to constrain our three parameters u, r and ρ . For this, we will take the projection of conservation equation on four velocity vectors, i.e., $u^{\mu}T^{\nu}_{\mu;\nu} = 0$ and obtain [53] as

$$ur^2 M^{-2} \exp\left\{ \int_{\rho_{\infty}}^{\rho} \frac{d\rho'}{\rho' + p(\rho')} \right\} = -\xi_2 = ux^2 \exp\left\{ \int_{\rho_{\infty}}^{\rho} \frac{d\rho'}{\rho' + p(\rho')} \right\} ,$$
 (45)

 $\xi_2 > 0$ symbolizes a constant related to the energy flux [53, 54, 55, 56]. Here ρ and ρ_{∞} respectively represent the values of the density at a finite distance and at an infinite distance. x is a dimensionless radial distance parameter.

Suppose the number density of the medium is n [55] then,

$$\frac{d\rho}{\rho + p} = \frac{dn}{n} \quad . \tag{46}$$

Integrating,

$$n \equiv n_{\infty} \exp\left\{ \int_{\rho_{\infty}}^{\rho} \frac{d\rho'}{\rho' + p(\rho')} \right\} \quad , \tag{47}$$

where n_{∞} is the concentration of DE [55] (42) and (44) evolves

$$\frac{\rho + p}{n}\sqrt{u^2 + f(r)} = \xi_3 = -\frac{\xi_1}{\xi_2} = \frac{\rho_\infty + p(\rho_\infty)}{n_\infty} \quad . \tag{48}$$

To determine ξ_2 which has the dimension of energy flux, effective sonic speed squared is evaluated as

$$v^{2} = \frac{n}{\rho + p} \frac{d(\rho + p)}{dn} - 1 \quad . \tag{49}$$

Differentiating equations (45) and (48) and using (47), we obtain

$$\frac{du}{u} \left[v^2 - \frac{u^2}{u^2 + f(r)} \right] + \frac{dx}{x} \left[2v^2 - \frac{xf'(r)}{2(f(r) + u)} \right] = 0 \quad . \tag{50}$$

From this equation, radial inward speed gradient can be calculated as a numerator to denominator ratio. The denominator will clearly vanish at some $x = x_c$ in the interval $(0, \infty)$ depending on the structure of f(r). However, to make the flow physical, numerator should vanish parallely. These two vanishing expressions give us the relations

$$u_c^2 = \frac{1}{4} x_c \frac{df}{dx} \Big|_{x=x_c} \quad \text{and} \tag{51}$$

$$v_c^2 = \frac{x_c}{x_c f'(x_c) + 4f(x_c)} \left. \frac{df'}{dx} \right|_{x = x_c} \tag{52}$$

Now, using equations (51) and (52), from (44) we have

$$\frac{\rho_c + p(\rho_c)}{\rho_\infty + p(\rho_\infty)} = \frac{\exp\left\{\int_{\rho_\infty}^\rho \frac{d\rho'}{\rho' + p(\rho')}\right\}}{2\sqrt{x_c \left.\frac{\partial f(x)}{\partial x}\right|_{x=x_c}} + 4f(x_c)}$$
(53)

We are able to calculate

$$\xi_2 = \frac{x_c^3}{2} \frac{df}{dx} \bigg|_{x=x_c} \times \exp\left\{ \int_{\rho_\infty}^{\rho_c} \frac{d\rho'}{\rho' + p(\rho')} \right\} \quad . \tag{54}$$

or,
$$\xi_2 = \frac{x_c^3}{2} \frac{df}{dx} \Big|_{x=x_c} \times \exp\left\{ \int_{\rho_\infty}^{\rho_c} \frac{d\rho'}{\rho' + (\omega_0 + \omega_1 z) \, \rho'} \right\}$$
 (55)

For different DE models, different values of ξ_2 (= ξ_2^{DE} say) can be obtained.

Using this, the rate of change of mass of the BH is calculated as

$$\dot{M} = -4\pi \xi_1 M^2 = 4\pi \xi_2 M^2 \left[\rho_\infty + p(\rho_\infty) \right] . \tag{56}$$

Several articles [57, 58, 59, 60, 61] suggest that the rate of change of mass can be calculated does not satisfy the dominant energy condition, whenever we can apply the EoS from equation (10).

Hence,

$$\dot{M} = 4\pi \xi_2 M^2 [\rho + p(\rho)] \quad . \tag{57}$$

Sign of \dot{M} is solely determined by that of $(\rho + p)$. For quintessence $-1 < \frac{p}{\rho} < -\frac{1}{3}$ and hence $\dot{M} > 0$. But once phantom barrier $\left(\frac{p}{\rho} = -1\right)$ is crossed, $p + \rho < 0$ and hence $\dot{M} < 0$.

$$\frac{dM}{d\rho} = -\frac{4\pi\xi_2 M^2}{3H^2} \Rightarrow \int_{M}^{M_0} \frac{dM}{M^2} = -\frac{4\pi\xi_2}{3} \int_{\rho}^{\rho_0} \frac{d\rho}{H} \Rightarrow \frac{1}{M} - \frac{1}{M_0} = -\frac{4\pi\xi_2}{3} \int_{\rho}^{\rho_0} \frac{d\rho}{H}$$

$$\Rightarrow M = \frac{M_0}{1 + \frac{4\pi\xi_2 M_0}{3} \int_{\rho}^{\rho_0} \frac{d\rho}{\sqrt{\frac{8\pi G_N}{3} \rho + \frac{\Lambda}{3} - \frac{\kappa}{a^2}}}} \quad . \tag{58}$$

Here $M_0\left(M(z=0)\right)$ is the present day mass of the BH. The ernergy density of present time $\rho(z=0)$ is constituted of three parts: the matter density of present time ρ_{m_0} , radiation density ρ_{rad_0} and the same for DE ρ_{DE_0} .

Hence we obtain

$$M = \frac{M_0}{1 + \frac{4\pi\xi_2 M_0}{3} \int_{\rho_0}^{\rho} \frac{d(\rho_b + \rho_{DE} + \rho_r)}{\sqrt{\frac{8\pi G_N}{3} (\rho_b + \rho_{DE} + \rho_r) + \frac{\Lambda}{3} - \frac{\kappa}{a^2}}}$$
 (59)

In figure 1d, $\log\left(\frac{M}{M_0}\right)$ vs z is plotted for LRP model $(\rho^{LRP}(z) = \rho_{\phi 0} \exp(3\omega_1 z)(1+z)^{3(1+\omega_0+\omega_1)})$. In past, i.e., for high redshift, almost 20% excess mass than today is observed. Mass started to get reduced as we shift towards the zero redshift. In a LRP, the observed decrease of $\log_{10}[M(z)/M_0]$ from 0.2 to 0 as z evolves from 2 to 0 suggests that the relative mass growth of BHs diminishes toward the present epoch, reflecting a gradual suppression of accretion efficiency. When the BH resides in a MCG background, this trend can be understood as a dynamical consequence of the evolving equation of state of the MCG: at

higher redshifts ($z \sim 2$), the MCG behaves like a matter like fluid, enabling efficient accretion, whereas at lower redshifts the transition to a negative pressure, DE like phase produces a repulsive effect that hinders infall. Consequently, the decline in $\log_{10}[M(z)/M_0]$ captures the cosmological shift from a dense, accretion dominated era to a DE dominated regime, consistent with the cosmic downsizing scenario of BH growth.

In figure 2d, $\log\left(\frac{M}{M_0}\right)$ is plotted with respect to z and we observe a steep fall towards origin. For the CPL DE parametrization $\rho_{\phi}^{CPL}(z) = \rho_{\phi 0}^{CPL}$ exp $\left\{-3w_1^{CPL}\frac{z}{1+z}\right\}(1+z)^{3\left(1+w_0^{CPL}+w_1^{CPL}\right)}$, a steep decline of BH mass in the past during accretion onto a MCG contaminated background indicates that the effective energy density of the surrounding fluid was dominated by a strongly negative pressure component. At high redshifts, the CPL form $\omega(z) = \omega_0 + \omega_1 z/(1+z)$ allows $\omega(z) < -1$, leading to a phantom like regime where the inflowing MCG exerts repulsive gravitational effects, causing a rapid decrease in BH mass. This behaviour reflects the nontrivial coupling between the dynamical DE sector and accreting matter, implying that the BH evolution is sensitive to both the background equation of state and its redshift evolution. Physically, this represents the extraction of gravitational energy by a fluid with supernegative pressure, violating the usual mass growth trend expected in standard accretion. Such a phenomenon indicates that in a DE dominated background, the thermodynamic balance between the BH and the cosmic fluid is altered, with the horizon effectively acting as an energy emitter rather than an absorber.

In figure 3d, log of BH mass to present time BH mass ratio is plotted as a function of redshift. For Linear and CPL, near origin slopes were less. For JBP $\left(\rho_{\phi}^{JBP}(z) = \rho_{\phi0}^{JBP}\right) \exp\left\{\frac{3w_1^{JBP}}{2(1+z)}\right\} (1+z)^{3(1+w_0^{JBP})}$ near origin slope is high. In an MCG dominated universe, the comparatively smaller near origin slopes for the Linear and CPL parametrizations imply that the DE equation of state evolves slowly at late times, producing a quasi-stationary background with weak pressure gradients around the BH. As a result, the inflow and outflow of energy across the horizon nearly balance, leading to a gentle and stable evolution of BH mass. However, the JBP parametrization, exhibiting a steep slope near the horizon, corresponds to a rapidly varying $\omega(z)$ at low redshift. This induces a stronger local pressure anisotropy in the MCG fluid, enhancing the energy flux and triggering a sharp change in the accretion dynamics. Physically, it suggests that in the JBP framework, DE interacts more actively with the BH environment, and the transition from matter-like to DE dominated behaviour produces a more violent mass evolution near the horizon.

For ERP
$$\left(\rho^{ERP}(z) = \rho_{\phi 0} \left(1+z\right)^{3\left\{1+\omega_0^{Log}+\frac{\omega_1^{Log}}{2}\log(1+z)\right\}}\right)$$
, we follow the mass of the BH to fall with

time. The pattern does match with that of LRP model. The resemblance between the $\log_{10}[M(z)/M_0]$ behaviour in the logarithmic and linear DE parametrizations arises from the fact that both models describe a gradual, smooth evolution of the equation of state $\omega(z)$ without introducing any sharp dynamical transitions in the cosmic background. In an MCG dominated universe, the accretion rate onto the BH is primarily governed by the pressure to density ratio of the surrounding fluid; hence, when $\omega(z)$ evolves linearly or logarithmically with redshift, the resulting pressure gradient and energy flux toward the horizon remain comparably weak and slowly varying. This leads to a nearly identical mass evolution profile because the effective gravitational potential around the BH changes adiabatically, maintaining thermodynamic equilibrium with the expanding MCG background. Physically, this implies that both parametrizations represent a cosmological regime where DE acts as a quasi-stationary, weakly dynamical field sufficient to drive acceleration but not strong enough to significantly disrupt the steady state accretion process of the BH.

FSLL-I $(\rho^{FSLL-I}(z) = \rho_{\phi 0} \exp\left[\frac{3 \, \omega_1^{FSLL-I}}{2} \left\{ \tan^{-1} \left(1 - \frac{2}{1+z}\right) + \pi/4 \right\} \right])$ presents similar pattern mass evolution curve as LRP or ERP. Only the magnitude is lesser than the previous two. When the same physical quantity, such as $\log_{10}[M(z)/M_0]$, appears roughly 0.1 order lower than in the linear or logarithmic parametrizations but follows an identical overall trend, it signifies that the underlying dynamical mechanism remains unchanged while the effective strength of the interaction is mildly suppressed. This small quantitative deviation reflects a reduction in the net energy flux across the BH horizon, caused by a slightly weaker coupling between the MCG background and the BH's gravitational field. Physically, the thermodynamic evolution, the balance between accretion and cosmic expansion, and the pressure gradient structure all evolve in the same manner, but with a lower amplitude of mass variation. Hence, the model preserves the qualitative behaviour of the linear/logarithmic forms, differing only in the efficiency of the energy transfer process that governs BH mass evolution.

$$\rho^{FSLL-II}(z) = \rho_{\phi 0} \exp\left[-\frac{3 \omega_1^{FSLL-II}}{2} \left\{ \tan^{-1} \left(1 - \frac{2}{1+z}\right) + \pi/4 \right\} \right]$$

$$(1+z)^{3(1+\omega_0^{FSLL-I} + \omega_1^{FSLL-II})} \left\{ 1 - \frac{2}{1+z} - \frac{2}{(1+z)^2} \right\}^{\frac{3\omega_1^{FSLL-II}}{4}}$$
(60)

In the FSLL-II parametrization (given in figure 5d, drawn with the help of the $\log_{10}[M(z)/M_0]$ mass ratio), reaching a minimum in the recent past before rising toward the present epoch reflects a profound interplay between BH accretion, cosmic expansion, and the evolving DE background. During the epoch of the minimum, the strongly negative pressure of the DE component, modeled here via the MCG, generates a repulsive gravitational effect that effectively reverses or stalls the inflow of energy across the BH horizon. This not only slows or temporarily decreases BH mass but also indicates a breakdown of the quasistatic thermodynamic balance at the horizon, as the negative pressure fluid injects an outward flux that competes with standard accretion. As the universe expands further, the EoS softens, reducing the repulsive effect and allowing gravitationally bound matter and residual MCG inflow to resume dominance, restoring accretion and increasing the mass ratio. Physically, this nonmonotonic behaviour illustrates how the BH horizon acts as a sensitive probe of the time dependent cosmic pressure landscape, capturing the dynamic transition from a DE dominated, repulsion suppressing phase to a matter like, accretion supporting regime. It highlights the intimate coupling between horizon thermodynamics, fluid dynamics of the cosmic medium, and large scale accelerated expansion, offering a unique window into the interplay of local strong gravity and global cosmological evolution.

Ploy-I and Poly-II parameterizations show more or less same patterns as the LRP or ERP models(in figures 7d and 8d).

$$\rho^{Poly-I} = \rho_{\phi 0} (1+z)^{\frac{3}{2}(1+10c_1^{Poly-I}+9c_2^{Poly-I})} \exp \left\{ \frac{3(5-16c_1^{Poly-I}-27c_2^{Poly-I})z}{4(1+z)} - \frac{9(1-3c_2c_2^{Poly-I})z(2+z)}{8(1+z)^2} \right\}$$

In figure 9d, we have plotted comparative mass growth for BA model. In recent past, around the $z \sim 0.3$, mass ratio is highest and then falls towards the origin. In the BA DE model, the $\log_{10}[M(z)/M_0]$ mass ratio reaching a maximum around $z \sim 0.3$ in the recent past before decreasing toward the present epoch indicates a transient enhancement of BH accretion driven by the evolving cosmic fluid. At this epoch, the equation of state $\omega(z)$ of the BA parametrization is such that the effective pressure of the surrounding

MCG or matter like component is minimized, producing a locally stronger gravitational inflow and a peak in energy flux across the BH horizon. As the universe continues to expand toward z = 0, the DE pressure increases, enhancing the repulsive effect and reducing the net accretion, which leads to a fall in the mass ratio. Physically, this behaviour highlights the sensitivity of BH growth to the detailed temporal evolution of the DE EoS, showing that even mild variations in $\omega(z)$ can transiently boost horizon accretion before repulsive effects dominate in the late time accelerated expansion era.

Fig 10d and 11d are for BAZS and ASSS model respectively and the curves resemble that for the LRP.

6 Conclusion

Black Hole Mass Evolution in Dark Energy Backgrounds: Summary of Parametrization Effects: The evolution of black hole mass in the presence of a cosmic fluid, particularly a MCG, is highly sensitive to the choice of DE EoS parametrization. Observables such as the logarithmic mass ratio, $\log_{10}[M(z)/M_0]$, provide insights into the interplay between local horizon physics and global cosmological expansion. Across different parametrizations, distinct trends emerge, reflecting how the evolving pressure and energy density of the cosmic fluid regulate accretion dynamics.

Linear, Logarithmic, and CPL Parametrizations: In linear $(\omega(z) = \omega_0 + \omega_1 z)$ and logarithmic parametrizations, the mass ratio evolves smoothly with redshift. Both exhibit gentle slopes near the present epoch $(z \sim 0)$, indicating that the DE EoS changes slowly, producing a quasi-stationary background where the inflow of energy toward the black hole remains moderate. The logarithmic parametrization, while slightly altering the functional form, produces nearly identical trends to the linear model, demonstrating that the accretion is governed primarily by the smooth, adiabatic variation of the MCG pressure. A small offset in amplitude (e.g., ~ 0.1 order less) can arise due to minor differences in effective energy flux, but the qualitative behaviour remains unchanged. The CPL parametrization $(\omega(z) = \omega_0 + \omega_1 z/(1+z))$ also shows slow mass evolution near the origin, reflecting weak late-time pressure gradients that maintain a nearly steady accretion flow.

JBP Parametrization: The Jassal–Bagla–Padmanabhan (JBP) model, in contrast, exhibits a steep slope near the horizon at low redshift, indicating a rapid change in the EoS $\omega(z)$ as the universe evolves. This produces a stronger local pressure anisotropy in the MCG fluid, enhancing energy flux and causing a more pronounced variation in the black hole mass. Physically, it reflects a regime where DE interacts more actively with the black hole environment, amplifying the sensitivity of accretion to the transition between matter-like and dark energy-dominated phases.

FSLL-II Parametrization: For FSLL-II, the mass ratio shows a non-monotonic behaviour, reaching a minimum in the recent past before increasing toward the present epoch. During the minimum, the strongly negative pressure of the dark energy component can temporarily suppress or even reverse accretion, effectively reducing the black hole mass. As the EoS softens with cosmic expansion, gravitationally bound matter and residual MCG inflow resume dominance, restoring accretion. This illustrates the extreme sensitivity of horizon thermodynamics to the time-dependent cosmic pressure landscape, where evolving dark energy can temporarily suppress and then revive mass growth.

Barboza–Alcaniz (BA) Model: In the BA parametrization, the $\log_{10}[M(z)/M_0]$ ratio peaks around $z \sim 0.3$ and declines toward z = 0. This peak corresponds to a transient epoch where the effective pressure of

the surrounding MCG or matter-like component is minimized, leading to a local enhancement in accretion. As the universe enters a more repulsive dark energy-dominated phase, the net inflow is reduced, and the mass ratio falls. This behaviour underscores how even subtle temporal variations in $\omega(z)$ can create transient boosts or suppressions in black hole growth.

Physical Interpretation Across Models: Across all parametrizations, key physical insights emerge:

- The slope and amplitude of $\log_{10}[M(z)/M_0]$ encode the local pressure gradients and energy flux at the black hole horizon, which are controlled by the evolving EoS $\omega(z)$ and the MCG properties.
- Non-monotonic behaviour (FSLL-II, BA) indicates epochs where repulsive dark energy temporarily dominates over gravitationally bound inflow, causing mass suppression or enhancement.
- Models with gentle slopes near the origin (Linear, Log, CPL) reflect adiabatic, quasi-static cosmic backgrounds, where dark energy evolves slowly and mass growth proceeds steadily.
- Steep slopes (JBP) signify rapid late-time evolution of the EoS, producing stronger local energy fluxes and more sensitive black hole growth.
- Minor amplitude shifts (e.g., 0.1 order) indicate changes in the effective accretion efficiency or flux without altering the qualitative trend.
- Overall, black hole mass evolution serves as a sensitive probe of the interplay between local strong gravity and global cosmic expansion, capturing the cumulative effects of accretion, mergers, and dark energy dynamics.

In a nutshell, The comparative study of dark energy parametrizations—Linear, Logarithmic, CPL, JBP, FSLL-II, and BA—within an MCG background reveals that both the slope and non-monotonic features of $\log_{10}[M(z)/M_0]$ carry deep physical meaning. Steep slopes indicate strong late-time dynamical effects, non-monotonic minima or maxima trace transitions in the repulsive gravitational influence of DE, and gentle slopes correspond to quasi-static accretion. Collectively, these results demonstrate that the evolution of black hole mass is a sensitive indicator of the time-dependent equation of state, the pressure-density interplay of the cosmic fluid, and the thermodynamic behaviour of black hole horizons in a universe dominated by both DM like and DE like components.

Acknowledgment

RB and FR thank Inter University Centre for Astronomy and Astrophysics (IUCAA), Pune, India, for granting Visiting Associateship. PB and SP thank the Department of Mathematics, Jadavpur University. And SD thanks the Department of Mathematics, The University of Burdwan, for different research facilities.

Data Availability Statement

Data sharing not applicable to this article as no datasets were generated or analysed during the current study.

Conflict of Interest

There are no conflicts of interest.

Funding Statement

There is no funding to report for this article.

Code/Software

No software/Coder was used in this study.

References

- [1] D. M. Scolnic, D. O. Jones, A. Rest, Y. C. Pan, R. Chornock, R. J. Foley, M. E. Huber, R. Kessler, G. Narayan, A. G. Riess, *et al.*, "The complete light-curve sample of spectroscopically confirmed sne ia from pan-starrs1 and cosmological constraints from the combined pantheon sample," *The Astrophysical Journal*, vol. 859, no. 2, p. 101, 2018.
- [2] U. Debnath, A. Banerjee, and S. Chakraborty, "Role of modified chaplygin gas in accelerated universe," Classical and Quantum Gravity, vol. 21, pp. 5609–5617, Nov 2004.
- [3] E. Babichev, V. Dokuchaev, and Y. N. Eroshenko, "The accretion of dark energy onto a black hole," Journal of Experimental and Theoretical Physics, vol. 100, no. 3, pp. 528–538, 2005.
- [4] B. Nayak and L. Singh, "Phantom energy accretion and primordial black holes evolution in brans-dicke theory," *The European Physical Journal C*, vol. 71, no. 12, p. 1837, 2011.
- [5] F. De Paolis, M. Jamil, and A. Qadir, "Black holes in bulk viscous cosmology," *International Journal of Theoretical Physics*, vol. 49, no. 3, pp. 621–632, 2010.
- [6] M. Jamil, A. Qadir, and M. A. Rashid, "Charged black holes in phantom cosmology," *The European Physical Journal C*, vol. 58, no. 2, pp. 325–329, 2008.
- [7] A. M. Ghez, S. Salim, N. N. Weinberg, J. R. Lu, T. Do, J. K. Dunn, K. Matthews, M. R. Morris, S. Yelda, E. E. Becklin, T. Kremenek, M. Milosavljevic, and J. Naiman, "Measuring distance and properties of the milky way's central supermassive black hole with stellar orbits," *The Astrophysical Journal*, vol. 689, no. 2, pp. 1044–1062, 2008.
- [8] P. S. Joshi and I. H. Dwivedi, "Naked singularities in spherically symmetric inhomogeneous tolman-bondi dust cloud collapse," *Physical Review D*, vol. 47, no. 10, pp. 5357–5369, 1993.
- [9] S. Akcay, "The kerr-de sitter universe," Classical and Quantum Gravity, vol. 28, no. 8, p. 085012, 2011.
- [10] S. G. Ghosh, "Rotating black hole and quintessence," *Physical Review D*, vol. 92, no. 10, p. 104042, 2015.
- [11] S. G. Ghosh, S. U. Islam, and S. D. Maharaj, "Rotating kiselev black holes in f(r,t) gravity," arXiv preprint, no. 2307.11611, 2023. arXiv:2307.11611 [gr-qc].
- [12] Y. Sekhmani, J. Rayimbaev, G. G. Luciano, R. Myrzakulov, and D. J. Gogoi, "Phase structure of charged ads black holes surrounded by exotic fluid with modified chaplygin equation of state," *European Physical Journal C*, vol. 84, no. 227, 2024.
- [13] B. Li, W. Xu, L. Wang, and K. Yang, "Black hole solutions in f(q) gravity," European Physical Journal C, vol. 82, no. 1, p. 51, 2022.
- [14] S. M. Carroll, Spacetime and Geometry: An Introduction to General Relativity. Addison Wesley, 2004.

- [15] M.-Y. Zhang, H. Chen, H. Hassanabad, Z.-W. Long, and H. Yang, "Critical behavior and joule-thomson expansion of charged ads black holes surrounded by exotic fluid with modified chaplygin equation of state," *Chinese Physics C*, vol. 48, no. 6, p. 065101, 2024.
- [16] M. Abramowitz and I. A. Stegun, eds., Handbook of Mathematical Functions with Formulas, Graphs, and Mathematical Tables, vol. 55 of Applied Mathematics Series. Washington, D.C.: U.S. Government Printing Office, 1965. National Bureau of Standards.
- [17] O. Farooq, F. R. Madiyar, S. Crandall, and B. Ratra, "Hubble parameter measurement constraints on the redshift of the deceleration-acceleration transition, dynamical dark energy, and space curvature," *The Astrophysical Journal*, vol. 835, no. 1, p. 26, 2017.
- [18] C. Zhang, H. Zhang, S. Yuan, S. Liu, T.-J. Zhang, and Y.-C. Sun, "Four new observational H(z) data from luminous red galaxies in the Sloan Digital Sky Survey data release seven," *Research in Astronomy and Astrophysics*, vol. 14, pp. 1221–1233, Oct. 2014.
- [19] M.-J. Zhang and J.-Q. Xia, "Test of the cosmic evolution using gaussian processes," *Journal of Cosmology and Astroparticle Physics*, vol. 2016, p. 005–005, Dec. 2016.
- [20] J. Simon, L. Verde, and R. Jimenez, "Constraints on the redshift dependence of the dark energy potential," *Phys. Rev. D*, vol. 71, p. 123001, 2005.
- [21] D. Stern, R. Jimenez, L. Verde, M. Kamionkowski, and S. A. Stanford, "Cosmic chronometers: constraining the equation of state of dark energy. I: H(z) measurements," *Journal of Cosmology and Astroparticle Physics*, vol. 2010, p. 008, Feb. 2010.
- [22] M. Moresco, A. Cimatti, R. Jimenez, L. Pozzetti, G. Zamorani, M. Bolzonella, J. Dunlop, F. Lamareille, M. Mignoli, H. Pearce, P. Rosati, D. Stern, L. Verde, E. Zucca, C. M. Carollo, T. Contini, J. P. Kneib, O. Le Fevre, S. J. Lilly, V. Mainieri, A. Renzini, M. Scodeggio, I. Balestra, R. Gobat, R. McLure, S. Bardelli, A. Bongiorno, K. Caputi, O. Cucciati, S. de la Torre, L. de Ravel, P. Franzetti, B. Garilli, A. Iovino, P. Kampczyk, C. Knobel, K. Kovač, J. F. Le Borgne, V. Le Brun, C. Maier, R. Pelló, Y. Peng, E. Perez-Montero, V. Presotto, J. D. Silverman, M. Tanaka, L. A. M. Tasca, L. Tresse, D. Vergani, O. Almaini, L. Barnes, R. Bordoloi, E. Bradshaw, A. Cappi, R. Chuter, M. Cirasuolo, G. Coppa, C. Diener, S. Foucaud, W. Hartley, M. Kamionkowski, A. M. Koekemoer, C. López-Sanjuan, H. J. McCracken, P. Nair, P. Oesch, A. Stanford, and N. Welikala, "Improved constraints on the expansion rate of the Universe up to z ~1.1 from the spectroscopic evolution of cosmic chronometers," Journal of Cosmology and Astroparticle Physics, vol. 2012, p. 006, Aug. 2012.
- [23] M. Moresco, A. Cimatti, R. Jimenez, L. Pozzetti, G. Zamorani, M. Bolzonella, F. Dunlop, A. F. Heavens, and L. V. et al., "Improved constraints on the expansion rate of the universe up to $z\sim 1.1$ from the spectroscopic evolution of cosmic chronometers," *Journal of Cosmology and Astroparticle Physics*, vol. 2012, no. 08, p. 006, 2012.
- [24] A. Gómez-Valent and L. Amendola, " H_0 from cosmic chronometers and Type Ia supernovae, with Gaussian Processes and the novel Weighted Polynomial Regression method," JCAP, vol. 04, p. 051, 2018.

- [25] E. Gaztanaga, A. Cabre, and L. Hui, "Clustering of Luminous Red Galaxies IV: Baryon Acoustic Peak in the Line-of-Sight Direction and a Direct Measurement of H(z)," Mon. Not. Roy. Astron. Soc., vol. 399, pp. 1663–1680, 2009.
- [26] C.-H. Chuang and Y. Wang, "Modelling the anisotropic two-point galaxy correlation function on small scales and single-probe measurements of h(z), da(z) and f(z) $\sigma 8(z)$ from the sloan digital sky survey dr7 luminous red galaxies," *Monthly Notices of the Royal Astronomical Society*, vol. 435, pp. 255–262, Aug 2013.
- [27] M. Moresco, "Raising the bar: new constraints on the hubble parameter with cosmic chronometers at $z \sim 2$," Monthly Notices of the Royal Astronomical Society: Letters, vol. 450, pp. L16–L20, Apr 2015.
- [28] S. Alam *et al.*, "The clustering of galaxies in the completed SDSS-III Baryon Oscillation Spectroscopic Survey: cosmological analysis of the DR12 galaxy sample," *Mon. Not. Roy. Astron. Soc.*, vol. 470, no. 3, pp. 2617–2652, 2017.
- [29] M. Moresco, L. Pozzetti, A. Cimatti, R. Jimenez, C. Maraston, L. Verde, D. Thomas, A. Citro, R. Tojeiro, and D. Wilkinson, "A 6% measurement of the hubble parameter at $z \sim 0.45$: direct evidence of the epoch of cosmic re-acceleration," *Journal of Cosmology and Astroparticle Physics*, vol. 2016, pp. 014–014, May 2016.
- [30] C. Blake, S. Brough, M. Colless, C. Contreras, W. Couch, S. Croom, D. Croton, T. M. Davis, M. J. Drinkwater, K. Forster, and et al., "The wigglez dark energy survey: joint measurements of the expansion and growth history atz; 1," *Monthly Notices of the Royal Astronomical Society*, vol. 425, pp. 405–414, Jul 2012.
- [31] A. L. Ratsimbazafy, S. I. Loubser, S. M. Crawford, C. M. Cress, B. A. Bassett, R. C. Nichol, and P. Väisänen, "Age-dating luminous red galaxies observed with the southern african large telescope," *Monthly Notices of the Royal Astronomical Society*, vol. 467, pp. 3239–3254, Feb 2017.
- [32] D. Stern, R. Jimenez, L. Verde, S. A. Stanford, and M. Kamionkowski, "Cosmic chronometers: Constraining the equation of state of dark energy. ii. a spectroscopic catalog of red galaxies in galaxy clusters," The Astrophysical Journal Supplement Series, vol. 188, p. 280–289, May 2010.
- [33] L. Anderson, E. Aubourg, S. Bailey, F. Beutler, V. Bhardwaj, M. Blanton, A. S. Bolton, J. Brinkmann, J. R. Brownstein, A. Burden, and et al., "The clustering of galaxies in the sdss-iii baryon oscillation spectroscopic survey: baryon acoustic oscillations in the data releases 10 and 11 galaxy samples," Monthly Notices of the Royal Astronomical Society, vol. 441, pp. 24–62, Apr 2014.
- [34] N. G. Busca, T. Delubac, J. Rich, S. Bailey, A. Font-Ribera, D. Kirkby, J.-M. Le Goff, M. M. Pieri, A. Slosar, E. Aubourg, and et al., "Baryon acoustic oscillations in the lyαforest of boss quasars," Astronomy & Astrophysics, vol. 552, p. A96, Apr 2013.
- [35] T. Delubac, J. E. Bautista, N. G. Busca, J. Rich, D. Kirkby, S. Bailey, A. Font-Ribera, A. Slosar, K.-G. Lee, M. M. Pieri, and et al., "Baryon acoustic oscillations in the lyαforest of boss dr11 quasars," Astronomy & Astrophysics, vol. 574, p. A59, Jan 2015.

- [36] A. Font-Ribera, D. Kirkby, N. Busca, J. Miralda-Escudé, N. P. Ross, A. Slosar, J. Rich, E. Aubourg, S. Bailey, V. Bhardwaj, and et al., "Quasar-lyman α forest cross-correlation from boss dr11: Baryon acoustic oscillations," *Journal of Cosmology and Astroparticle Physics*, vol. 2014, pp. 027–027, May 2014.
- [37] D. J. Eisenstein, I. Zehavi, D. W. Hogg, R. Scoccimarro, M. R. Blanton, R. C. Nichol, R. Scranton, H. Seo, M. Tegmark, Z. Zheng, S. F. Anderson, J. Annis, N. Bahcall, J. Brinkmann, S. Burles, F. J. Castander, A. Connolly, I. Csabai, M. Doi, M. Fukugita, J. A. Frieman, K. Glazebrook, J. E. Gunn, J. S. Hendry, G. Hennessy, Z. Ivezić, S. Kent, G. R. Knapp, H. Lin, Y. Loh, R. H. Lupton, B. Margon, T. A. McKay, A. Meiksin, J. A. Munn, A. Pope, M. W. Richmond, D. Schlegel, D. P. Schneider, K. Shimasaku, C. Stoughton, M. A. Strauss, M. SubbaRao, A. S. Szalay, I. Szapudi, D. L. Tucker, B. Yanny, and D. G. York, "Detection of the baryon acoustic peak in the large-scale correlation function of sdss luminous red galaxies," The Astrophysical Journal, vol. 633, p. 560–574, Nov. 2005.
- [38] N. Aghanim, Y. Akrami, M. Ashdown, J. Aumont, C. Baccigalupi, M. Ballardini, A. J. Banday, R. B. Barreiro, N. Bartolo, S. Basak, R. Battye, K. Benabed, J.-P. Bernard, M. Bersanelli, P. Bielewicz, J. J. Bock, J. R. Bond, J. Borrill, F. R. Bouchet, F. Boulanger, M. Bucher, C. Burigana, R. C. Butler, E. Calabrese, J.-F. Cardoso, J. Carron, A. Challinor, H. C. Chiang, J. Chluba, L. P. L. Colombo, C. Combet, D. Contreras, B. P. Crill, F. Cuttaia, P. de Bernardis, G. de Zotti, J. Delabrouille, J.-M. Delouis, E. Di Valentino, J. M. Diego, O. Doré, M. Douspis, A. Ducout, X. Dupac, S. Dusini, G. Efstathiou, F. Elsner, T. A. Enßlin, H. K. Eriksen, Y. Fantaye, M. Farhang, J. Fergusson, R. Fernandez-Cobos, F. Finelli, F. Forastieri, M. Frailis, A. A. Fraisse, E. Franceschi, A. Frolov, S. Galeotta, S. Galli, K. Ganga, R. T. Génova-Santos, M. Gerbino, T. Ghosh, J. González-Nuevo, K. M. Górski, S. Gratton, A. Gruppuso, J. E. Gudmundsson, J. Hamann, W. Handley, F. K. Hansen, D. Herranz, S. R. Hildebrandt, E. Hivon, Z. Huang, A. H. Jaffe, W. C. Jones, A. Karakci, E. Keihänen, R. Keskitalo, K. Kiiveri, J. Kim, T. S. Kisner, L. Knox, N. Krachmalnicoff, M. Kunz, H. Kurki-Suonio, G. Lagache, J.-M. Lamarre, A. Lasenby, M. Lattanzi, C. R. Lawrence, M. Le Jeune, P. Lemos, J. Lesgourgues, F. Levrier, A. Lewis, M. Liguori, P. B. Lilje, M. Lilley, V. Lindholm, M. López-Caniego, P. M. Lubin, Y.-Z. Ma, J. F. Macías-Pérez, G. Maggio, D. Maino, N. Mandolesi, A. Mangilli, A. Marcos-Caballero, M. Maris, P. G. Martin, M. Martinelli, E. Martínez-González, S. Matarrese, N. Mauri, J. D. McEwen, P. R. Meinhold, A. Melchiorri, A. Mennella, M. Migliaccio, M. Millea, S. Mitra, M.-A. Miville-Deschênes, D. Molinari, L. Montier, G. Morgante, A. Moss, P. Natoli, H. U. Nørgaard-Nielsen, L. Pagano, D. Paoletti, B. Partridge, G. Patanchon, H. V. Peiris, F. Perrotta, V. Pettorino, F. Piacentini, L. Polastri, G. Polenta, J.-L. Puget, J. P. Rachen, M. Reinecke, M. Remazeilles, A. Renzi, G. Rocha, C. Rosset, G. Roudier, J. A. Rubiño-Martín, B. Ruiz-Granados, L. Salvati, M. Sandri, M. Savelainen, D. Scott, E. P. S. Shellard, C. Sirignano, G. Sirri, L. D. Spencer, R. Sunyaev, A.-S. Suur-Uski, J. A. Tauber, D. Tavagnacco, M. Tenti, L. Toffolatti, M. Tomasi, T. Trombetti, L. Valenziano, J. Valiviita, B. Van Tent, L. Vibert, P. Vielva, F. Villa, N. Vittorio, B. D. Wandelt, I. K. Wehus, M. White, S. D. M. White, A. Zacchei, and A. Zonca, "Planck2018 results: Vi. cosmological parameters," Astronomy & Astrophysics, vol. 641, p. A6, Sept. 2020.
- [39] Y. Wang and S. Wang, "Distance priors from planck and dark energy constraints from current data," *Physical Review D*, vol. 88, Aug. 2013.

- [40] D. L. Shafer, "Robust model comparison disfavors power law cosmology," Phys. Rev. D, vol. 91, no. 10, p. 103516, 2015.
- [41] R. Jimenez and A. Loeb, "Constraining cosmological parameters based on relative galaxy ages," *The Astrophysical Journal*, vol. 573, pp. 37–42, jul 2002.
- [42] Y. Wang and P. Mukherjee, "Observational constraints on dark energy and cosmic curvature," *Physical Review D*, vol. 76, Nov. 2007.
- [43] A. R. Cooray and D. Huterer, "Gravitational lensing as a probe of quintessence," *The Astrophysical Journal*, vol. 513, pp. L95–L98, March 1999.
- [44] M. Chevallier and D. Polarski, "Accelerating universes with scaling dark matter," *International Journal of Modern Physics D*, vol. 10, no. 2, p. 213–224, 2001.
- [45] H. Çalışkan et al., "Elemental abundance analysis of the magnetic chemically peculiar star hr 8216," Monthly Notices of the Royal Astronomical Society, vol. 356, no. 4, p. 1256–1262, 2005.
- [46] S. Perlmutter, M. S. Turner, and M. White, "Constraining dark energy with sne ia and large-scale structure," *Physical Review Letters*, vol. 83, p. 670–673, 1999. arXiv:astro-ph/9901052v2.
- [47] C.-J. Feng, X.-Y. Shen, P. Li, and X.-Z. Li, "A new class of parametrization for dark energy without divergence," *Journal of Cosmology and Astroparticle Physics*, vol. 2012, p. 023, September 2012.
- [48] I. Sendra and R. Lazkoz, "Supernova and baryon acoustic oscillation constraints on (new) polynomial dark energy parametrizations: current results and forecasts," *Monthly Notices of the Royal Astronomical Society*, vol. 422, pp. 776–793, April 2012.
- [49] E. M. Barboza and J. S. Alcaniz, "A parametric model for dark energy," *Physics Letters B*, vol. 666, pp. 415–419, September 2008.
- [50] E. M. Barboza, J. S. Alcaniz, Z.-H. Zhu, and R. Silva, "Generalized equation of state for dark energy," Physical Review D, vol. 80, p. 043521, August 2009.
- [51] U. Alam, V. Sahni, T. D. Saini, and A. A. Starobinsky, "Is there supernova evidence for dark energy metamorphosis?," Monthly Notices of the Royal Astronomical Society, vol. 354, pp. 275–291, October 2004.
- [52] U. Alam, V. Sahni, and A. A. Starobinsky, "The case for dynamical dark energy revisited," Journal of Cosmology and Astroparticle Physics, vol. 2004, p. 008, June 2004.
- [53] U. Debnath, "Accretion and Evaporation of Modified Hayward Black Hole," Eur. Phys. J. C, vol. 75, p. 129, 2015.
- [54] E. Babichev, V. Dokuchaev, and Y. Eroshenko, "Black hole mass decreasing due to phantom energy accretion," *Phys. Rev. Lett.*, vol. 93, p. 021102, 2004.
- [55] E. Babichev, V. Dokuchaev, and Y. Eroshenko, "The Accretion of dark energy onto a black hole," *J. Exp. Theor. Phys.*, vol. 100, pp. 528–538, 2005.

- [56] E. O. Babichev, V. I. Dokuchaev, and Y. N. Eroshenko, "Black holes in the presence of dark energy," Phys. Usp., vol. 56, pp. 1155–1175, 2013.
- [57] G. Abbas, "Phantom energy accretion onto a black hole in Hořava-Lifshitz gravity," Sci. China Phys. Mech. Astron., vol. 57, pp. 604–607, 2014.
- [58] E. Babichev, S. Chernov, V. Dokuchaev, and Y. Eroshenko, "Perfect fluid and scalar field in the Reissner-Nordstrom metric," *J. Exp. Theor. Phys.*, vol. 112, pp. 784–793, 2011.
- [59] M. Jamil and I. Hussain, "Accretion of phantom energy and generalized second law of thermodynamics for einstein-maxwell-gauss-bonnet black hole," *International Journal of Theoretical Physics*, vol. 50, p. 465–472, Nov. 2010.
- [60] M. Jamil and M. Akbar, "Generalized second law of thermodynamics for a phantom energy accreting btz black hole," *General Relativity and Gravitation*, vol. 43, p. 1061–1068, June 2010.
- [61] S. Dutta and R. Biswas, "Dark energy accretion onto van der waal's black hole," Communications in Theoretical Physics, vol. 71, p. 209, Feb. 2019.